minerals

MDPI

Article

Phosphate Record in Pleistocene-Holocene Sediments from Denisova Cave: Formation Mechanisms and Archaeological Implications

Ella V. Sokol [1], Maxim B. Kozlikin [2,3,*], Svetlana N. Kokh [1], Anna V. Nekipelova [1], Natalya A. Kulik [2], Viktoria A. Danilovsky [1], Pavel V. Khvorov [4] and Michael V. Shunkov [2]

[1] V.S. Sobolev Institute of Geology and Mineralogy Siberian Branch Russian Academy of Sciences, 3 Acad. Koptyug Avenue, 630090 Novosibirsk, Russia; sokol@igm.nsc.ru (E.V.S.); zateeva@igm.nsc.ru (S.N.K.); nekipelova@igm.nsc.ru (A.V.N.); vdanilovsky@igm.nsc.ru (V.A.D.)
[2] Institute of Archaeology and Ethnography Siberian Branch Russian Academy of Sciences, 17 Acad. Lavrentiev Avenue, 630090 Novosibirsk, Russia; kulik@archaeology.nsc.ru (N.A.K.); shunkov77@gmail.com (M.V.S.)
[3] ArchaeoZOOlogy in Siberia and Central Asia—ZooSCAn, CNRS—IAET SB RAS International Research Laboratory, IRL 2013, 630090 Novosibirsk, Russia
[4] South Urals Federal Research Center of Mineralogy and Geoecology, Ural Branch of the Russian Academy of Sciences, Ilmeny Reserve, 456317 Miass, Russia; khvorov@mineralogy.ru
* Correspondence: kmb777@yandex.ru

Abstract: The distribution of authigenic phosphates in the sedimentary sequence of prehistoric Denisova Cave (Altai, South Siberia) has important archeological implications. The sampled Late Pleistocene–Early Holocene sedimentary sequence in the East Chamber of the cave consists of argilo-sandy-phosphatic sediments intercalated with guano layers of insectivorous bats. The sediments bear partially degraded N-rich organic matter (OM); chitin fragments enriched in S, P, Zn, and Cu; and a set of phosphates. The guano layers record at least three prolonged episodes of cave occupation by colonies of insectivorous bats between 10 kyr and 5 kyr BP, after people had left the cave or visited it rarely in small groups. The formation of phosphates follows the OM biodegradation pathways, with acidic leaching and gradual neutralization of P-rich solutions. The depth profile of authigenic phosphates shows a suite of mineral assemblages that mark a trend from acidic to slightly alkaline pH conditions of guano degradation (from top to bottom): ardealite, taranakite, and leucophosphite corresponding to acidic environments; whitlockite, brushite, and hydroxylapatite, which are stable under slightly acidic and neutral conditions; and hydroxylapatite in coexistence with calcite and stable at the bottom of the leaching profile under alkaline conditions. Authigenic phosphates can be used as reliable indicators of human non-occupation (abandonment) periods of Denisova Cave. Acidic leaching is responsible for disturbance and/or elimination of archaeological and paleontological materials in Late Pleistocene–Early Holocene sediments that were exposed to at least three "acidic waves".

Keywords: authigenic phosphates; bat guano; acidic leaching; ardealite; taranakite; brushite; whitlockite; prehistoric cave; Denisova Cave; Holocene

Citation: Sokol, E.V.; Kozlikin, M.B.; Kokh, S.N.; Nekipelova, A.V.; Kulik, N.A.; Danilovsky, V.A.; Khvorov, P.V.; Shunkov, M.V. Phosphate Record in Pleistocene-Holocene Sediments from Denisova Cave: Formation Mechanisms and Archaeological Implications. *Minerals* **2022**, *12*, 553. https://doi.org/10.3390/min12050553

Academic Editor: Yannicke Dauphin

Received: 22 March 2022
Accepted: 24 April 2022
Published: 28 April 2022

1. Introduction

Chemical processes that change the composition of both exposed and buried soils and sediments, including cave deposits, have received much recent attention [1–8]. Such studies provide insights into soil processes (acidification, salinization, oxidation, and hydration) controlled by landscape, climate, and microbial factors. These data and the inferred trends of thermodynamic parameters have archaeological implications because

environmental changes implicitly or explicitly affect the biological and cultural evolution of humans [2,9,10].

Postdepositional chemical reactions between mineral, organic, and other components of sediments leached by percolating solutions cause dramatic effects on the composition and structure of archaeological remains and disturb cultural layers and their stratigraphy. As leaching progresses, sedimentary beds change in volume, coalesce, and loose lithological boundaries and primary bedding, whereby archaeological and organic remains become offset. On the other hand, false bedding may appear as reaction interfaces and geochemical barriers. Therefore, identifying and taking into account postdepositional changes is critical to avoid misinterpretation of sedimentary records [2,11].

Postdepositional chemical agents can either preserve or destroy paleontological, anthropological, or other organic remains, for instance, fossilization of bones and teeth relevant to archeological problems and biodegradation. Fossilization is associated with profound changes in both the chemistry and structure of tissues and includes bulk recrystallization of original biogenic Ca-phosphates, as well as uptake of elements, including trace elements, by bones [12–16]. Microbial degradation of bone material leads to a local pH decrease in pore waters and dissolution of biogenic Ca phosphates [17–21].

Dissolution and chemical changes in sediments and the archaeological materials they host can be detected using mineral indicators, but the ways of using mineral species other than apatite in this respect remain poorly investigated. There are two basic approaches to the estimation of the chemical changes to archaeologically significant materials (bones, teeth, phytoliths, pollen, plant detritus, and charcoal) and their sedimentary hosts [2]:

i. Reconstructing the paleochemistry of archaeological sediments in order to estimate the preservation of remains in a given environment after deposition and during diagenesis;
ii. Detecting secondary indicators that appeared and/or survived during diagenesis being stable in the altered environment and justifying their suitability for interpretation of past conditions and events.

Bacterial and, to a lesser extent, fungal degradation of bat guano in prehistoric caves is among the key driving forces of chemical alteration of sediments and related authigenic mineralization. Phosphates are among the most common, widespread, and manifold authigenic minerals (about sixty mineral species) that form in caves due to the availability of phosphorus released in the process of guano biodegradation. These minerals form by interaction of clayey matter, aluminous silicate rocks, and/or limestone with solutions enriched in phosphate derived from bat or bird guano or, less commonly, bones [1,3,4,22–24]. Recently studied cave phosphate species include taranakite $(K,Na,NH_4)_3(Al,Fe^{3+})_5(HPO_4)_6(PO_4)_2{\cdot}18H_2O$; leucophosphite $(KFe^{3+}{}_2(PO_4)_2(OH){\cdot}2H_2O)$; tinsleyite $(K(Al,Fe)_2(PO_4)_2(OH){\cdot}2H_2O)$; variscite $(Al(PO_4){\cdot}2H_2O)$; crandallite $(CaAl_3(PO_4)_2(OH)_5{\cdot}H_2O)$; ardealite $(Ca_2(SO_4)(HPO_4){\cdot}4H_2O)$; brushite $(CaHPO_4{\cdot}2H_2O)$; whitlockite $(Ca_9(Mg,Fe^{2+})(PO_4)_6(HPO_4))$; and montgomeryite $(Ca_4(Mg,Fe)Al_4(PO_4)_6(OH)_4{\cdot}12H_2O)$, as well as X-ray-amorphous or poorly crystalline carbonate-hydroxylapatite, also known as dahllite $(Ca_5(PO_4,CO_3)_3(OH))$.

Caves throughout the world are often inhabited by large populations of insectivorous and/or fruit bats in the absence of humans. Thus, fecal (guano) layers in cave deposits can be used as reliable indicators of human non-occupation periods; however, they degrade in a few decades, especially in wet caves located in warm climate zones, and may disappear from prehistoric caves after bat colonies leave [1,3]. However, degraded bat guano leaves a record in the form of particular geochemical and mineralogical profiles with specific authigenic phosphate minerals that form via the interaction of cave sediments with compositionally complex acidic solutions released in the process of guano biodegradation. The phosphatic suites, as well as selected minerals and/or mineral assemblages, may be useful to constrain the periods of human non-occupation in prehistoric caves. A

phosphatic sequence in Pleistocene and Holocene sediments of the East Chamber in Denisova Cave (Altai, Russia) is the focus of the present study.

2. Denisova Cave

2.1. Historic Background

Denisova Cave in the Russian Altai (southwestern Siberia) is a key site for understanding the complex relationships between hominin groups that inhabited Eurasia in the Middle and Late Pleistocene epochs. DNA sequenced from human remains from the Denisova site revealed the presence of a hitherto unknown hominin group, the Denisovans [25–27], and high-coverage genomes from both Neanderthal and Denisovan fossils provide evidence for admixture between these two populations [28]. The cave was discovered as a multilayer archaeological site in 1977 by paleontologist N. Ovodov [29]. A wealth of Middle Paleolithic to Medieval archaeological materials has already been obtained from two first test pits in the entrance area and the Main Chamber of the cave.

The cave sediments were sampled at different depths and in different parts of the cave during several field campaigns: Holocene sediments from the Main Chamber and entrance area in 1982 and 1983 [30]; Pleistocene sediments from the Main Chamber in 1984, 1993–1995, 1997, and 2016, when eight Holocene and fourteen Pleistocene continuously numbered units (1 through 22) were distinguished in the cave section [31]; Pleistocene sediments from the entrance area in 1990, 1991, and 1996, with fifteen distinguished lithological units; samples from an excavation near the entrance of the South Chamber in 1999–2003, the same stratigraphic units as in the Main Chamber [31]; Holocene and Pleistocene deposits from the entrance area and the East Chamber in 2004–2016, with independent numbering of lithological units. Different sections of the cave were correlated in previous publications [9,32].

2.2. Geological and Archaeological Background

Denisova Cave (51°23′51.3″ N, 84°40′34.3″ E) is located in the northwestern Altai in the upper reaches of the Anui River, within 5 km of Cherny Anui Village on its right side (Figure 1a). The upper Anui valley strikes in the SE–NW direction between the Bashchelak (2000–2200 m) and Anui (1200–1500 m) ranges and opens northward into the Altai foothills. In the south, it is separated from the Kan intermontane basin by a series of N–S ranges (Chichke, Usunbut, and Leshiktu), rising from 1200 to 1600 m asl. The floor of the Anui valley at the cave site is 120 m wide. The cave mouth is located at the foot of a rocky scrap, at 690 m asl, 28 m above the lowest stand of the Anui River (662 m asl). It looks southwest and is 6 m high and 7 m wide [9]; however, it was much lower (≤1.7 m) and narrower prior to excavation, which made the cave space more isolated from external effects.

Denisova Cave is one of about sixty caves, grottos, and sink holes in the Anui karst region [33,34]. It is a horizontal cave, a typical example of a near-surface karst, in a large block of Silurian (Upper Llandovery) reef limestone with very sporadic pyrite mineralization [33] (Figure 1b). The cave formed by successive and/or concurrent action of three independent factors [35]: chemical weathering (karst formation proper, i.e., initiation of caves before the exit to the Anui River opened); chemical weathering and mechanic wear (joint effect of karst formation and erosion by the river the in pre-Late Pleistocene); and corrosion, biogenic, and anthropogenic processes (combination of karst formation and degraded waste products of animals and humans, Late Pleistocene-Holocene).

Altogether, 110 m of cave chambers and tunnels over an area of 270 m^2 were explored; the cave volume was 330 m^3 before the excavations. The cave consists of short, quasi-horizontal or gently dipping chambers connected via the NW-oriented Main Chamber. One SW chamber opens into the entrance area, and two narrow, dark chambers strike SE inward in the karst, where they are fully buried under soft sediments. The East Chamber, farthest from the entrance (Figure 2a–c), was excavated over a 9 m long, 10 m high,

and ~3 m wide space. It was originally filled with soft sediments that underwent postdepositional viscoplastic deformation, but no mixing of material from different lithological units occurred. Thus, it was possible to trace the boundaries of archaeostratigraphic units, correlate them to lithostratigraphic units, and sample for spore-pollen analysis [9,36].

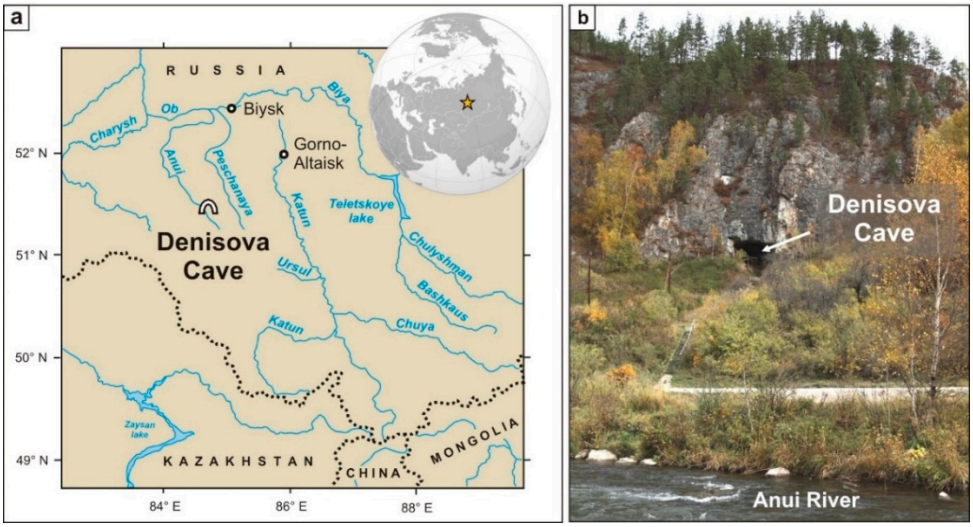

Figure 1. Location map of study area (Gorny Altai, Russia) (**a**) and general view of the Denisova Cave mouth (**b**).

The Main Chamber in the center of the cave is dome-shaped, reaching 9–11 m in diameter and ~10 m in height above the sediment surface, and has a ~1 m open hole in the ceiling in the southern part. The hole illuminates this largest and most comfortable space of the cave and serves as a chimney with good draft, especially in winter. The Main Chamber remains dry over the greatest part of the year, except for summer, when moisture condensates on the walls. The walls are smooth and cut by steep to gently dipping fractures controlling the geometry of chambers and tunnels. No fractures formed or rejuvenated while we were working [9,33].

Year-round temperature monitoring in Denisova Cave was performed in 2002–2004, (after its mouth had already been broadened [37]) at four points inside the cave and four points in its vicinity. The monitoring showed that the temperatures in the cave spaces away from the entrance are more comfortable than outside from November to February, with a range of −13 to +1 °C. From May through September, the temperatures outside the cave are more favorable than inside: −7 to +40 °C and −6 to +13 °C, respectively. The size and geometry of the chambers and tunnels have not changed much since the Pleistocene, and the rock lithology, as a control of thermal conductivity, has been invariable. Therefore, the general temperature trend in the Pleistocene and Holocene was similar to that obtained by the monitoring, though the difference in temperatures inside and outside the cave varied over the year. The favorable temperature regime inside the cave could last from October to March or April during the Pleistocene cooling (MIS 2). The temperature in the cave interior was less variable before the entrance became broader, when it was better isolated, especially in the East Chamber. At present, bats seasonally occupy the caves of southern Siberia (during winter) at an optimal temperature of 8 to 0 °C [38–40].

Like most Altai caves in limestone, speleothems in Denisova Cave [9,33] are few and limited to fragments of broken stalactites in basal beds of sediments and a small stalagmite fully replaced by Ca phosphates near the western wall of the East Chamber (unit 6). Therefore, the cave has been relatively dry, possibly with brief episodes of infiltration fluxes, which left no traces. In general, Denisova Cave can be classified as relatively warm and dry according to its morphology and microclimate.

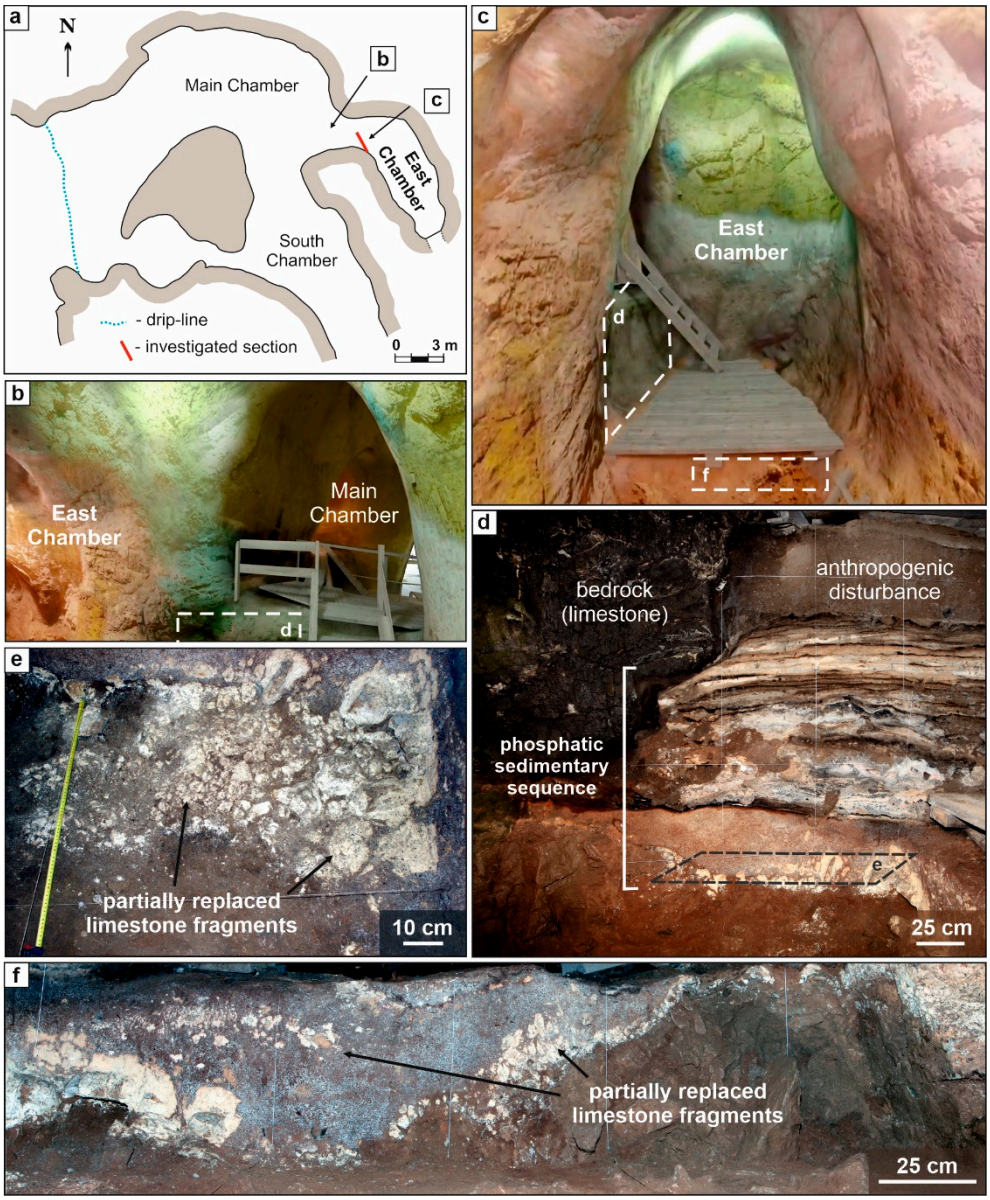

Figure 2. Denisova Cave plan and images of East Chamber showing excavated areas. (**a**) Plan view of Denisova Cave. (**b**,**c**) 3D images of East Chamber [41]. (**d**) Profile view of excavated phosphatic sedimentary sequence in the East Chamber. (**e**,**f**) Totally and partially replaced limestone fragments at the base of phosphatic sedimentary sequence (layers 11.1 and 11.2): view from above (**e**) and cross section (**f**).

3. Authigenic Phosphates in Cave Sediments

The human occupation of caves can be commonly inferred from the presence of anthropogenic signatures in cave deposits of certain ages, but the absence of artefacts in a cave does not necessarily mean that humans never lived there. Bones, teeth, and even stone tools could become dissolved or altered by postdepositional chemical reactions in the host sediments [2]. There is also other evidence of occupation in caves or their parts (tunnels, chambers, etc.). Cave spaces often housed large populations of insectivorous bats for prolonged winter or night stays, and their waste products (guano) accumulated immediately below the roost place [1,3].

Guano deposition is believed to be the most important agent of phosphate enrichment of cave sediments, as well as some insular sediment and ornithogenic soils, producing a number of Al-bearing phosphate minerals [1,2,20,42,43]. Guano is a byproduct of animal excretion, and its characteristics depend on the type of animal and its feeding

habits. The deposition rate of bat guano varies from 2 to 10 cm per year, and the total thickness of deposits can reach a few meters. Main constituents of fresh insectivorous bat guano are organic matter and water (83–94 wt%), with the contents of nitrogen and phosphorus ranging from 8 to 12 wt% and 2 to 7 wt%, respectively. Incinerated samples contain up to 36–43 wt% P_2O_5 and 9–14 wt% N_2O, whereas organic matter is rich in sulfur (from 2.5 to 24.3 wt%) [3]. Fresh bat guano studied in caves of Israel, Malaysia, and Philippines is composed of finely comminuted insect exoskeletons, the main structural component of which is chitin; bears traces of clay material, microscopic crystals of brushite, and 25–57 wt% phosphate matter; and has a slightly acidic reaction in aqueous solutions. Incinerated samples consist mainly of unidentified phosphate and ammonium sulfate [1,3].

Biodegradation of guano completes in tens of years, depending on the local climate [1,3]. The process begins with oxidation of organic compounds and mass loss on account of CO_2 and H_2O or, to a lesser extent, NH_3 [3,24,44]. The bacterial degradation produces organic acids and reduces pH of pore water to 4 [1,45]. Organic acids act as aggressive leaching agents and dissolve proteins, whereby $(PO_4)^{3-}$ and $(HPO_4)^{2-}$ pass to solution. Active bacterial processes likewise lead to enrichment of the degrading guano layer in HNO_3 salts—mainly nitranite ($NaNO_3$), which is a short-living, highly soluble compound—and sulfates in the lower portion of HSO_4 salts.

Complete degradation of bat guano leaves only a 1–2 cm layer of clay and quartz, which is hard to identify unambiguously [1]. In this respect, sediments containing authigenic phosphates can be reliable indicators of cave occupation by insectivorous bats. Their upper limit in the section of cave deposits approximately marks the primary position of the guano layer and, correspondingly, the stratigraphic level of the corresponding deposition and the time when people abandoned the cave. Authigenic phosphates deposited below the degrading guano layer make up a suite controlled by the general trend of original rapid decrease and subsequent gradual increase of pH from 2.7–4.1 to 7.1–8.0 while organic matter is decaying. Active guano deposition and onset of its degradation produce acidic solutions equilibrated with several Al- and/or Fe^{3+}-bearing phosphates in shales: variscite ($Al(PO_4)\cdot 2H_2O$); tinsleyite ($K(Al,Fe)_2(PO_4)_2(OH)\cdot 2H_2O$); leucophosphite ($KFe^{3+}{}_2(PO_4)_2(OH)\cdot 2H_2O$)l and their NH_4-rich analog, spheniscidite ($(NH_4,K)(Fe^{3+},Al)_2(PO_4)_2(OH)\cdot 2H_2O$), as well as taranakite ($(K,Na,NH_4)_3(Al,Fe^{3+})_5(HPO_4)_6(PO_4)_2\cdot 18H_2O$). Ardealite, a sulfate phosphate ($Ca_2(SO_4)(HPO_4)\cdot 4H_2O$), may form early during the process in limestone of dry caves and sometimes coexists with gypsum ($CaSO_4\cdot 2H_2O$) (Table 1).

Table 1. General characteristics of typical guano-related phosphates from archeological and non-archaeological cave sites.

Association	Aggregate Type	Features	Genesis	Cave Sites
Hydroxylapatite (carbonate-rich hydroxylapatite or dahllite) $Ca_5(PO_4,CO_3)_3(OH)$ hexagonal				
Cal **Gp** Bsh Adl	(i) Massive aggregates and crusts covering fragments of carbonate host rock (ii) Nodules and veins in the guano layer (iii) Pseudomorph after bones	(i) Carbonate-, sulfate- and Zn-bearing (ii) Low crystallinity	Interaction between near neutral phosphatic solution and $CaCO_3$	IL: Kebara *, Etzba * and Ornit * [1] IT: Arene Candide *, Cocci, Salnitro, Eremita and Apulian Caves [24,46,47] AU: Robertson * [48] RO: Cioclovina *, Măgurici, Mare de la Mereşti, Gura Dobrogei and Huda lui Papară [49–53]
Brushite $CaHPO_4\cdot 2H_2O$ monoclinic				
Ap **Cal** Adl Gp	(i) Crusts, nodules, veins in the guano layer (ii) Crusts over fragments of carbonate host rock or aggregates of hydroxylapatite	Sulfate-bearing	Interaction between slightly acidic phosphatic solution and $CaCO_3$	RO: Cioclovina *, Măgurici, Mare de la Mereşti, Gura Dobrogei and Huda lui Papară [49–54] ES: Serres Centrals [24] FR: Raganeous [24] IT: Salnitro and Apulian Caves [24,46]

				SV: Lighthouse, Reckley Hill, Midget Horror and Crescent Top [55]
Monetite $CaHPO_4$ triclinic				
Bsh **Bss** Fan	(i) Dispersed grains in guano-limestone sequence (ii) Pseudomorph after brushite	No data	(i) Dehydration of brushite in dry condition (ii) Dehydration of brushite due to microbial exothermic reactions	RO: Măgurici and Gura Dobrogei [49,52] SV: Lighthouse and Dance Hall [55]
Whitlockite $Ca_9(Mg,Fe^{2+})(PO_4)_6(HPO_4)$ trigonal				
Ap	(i) Powdered aggregates on carbonate rock surface (ii) Pseudomorph after bones	Sulfate-bearing	(i) Interaction between acidic phosphatic solution and Mg-calcite or dolomite (ii) Dissolution of apatite and subsequent precipitation from low-Ca solutions	MY: Niah [3] FR: Guano [24] SV: Lighthouse, Reckley Hill and Altar [55] AU: Wooltana [56]
Ardealite $Ca_2(SO_4)(HPO_4)\cdot 4H_2O$ monoclinic				
Gp **Bsh** **Ap**	(i) Crusts and intergranular pore infillings in sulfate-phosphate mineral aggregates (ii) Powdery material near the guano-limestone contact	No data	Interaction between acidic phosphatic solution and $CaCO_3$	IL: Ornit * [1] SV: Lighthouse [55] RO: Cioclovina *, Măgurici, Mare de la Mereşti, Gura Dobrogei and Huda lui Papară [49–57]
Crandallite $CaAl_3(PO_4)_2(OH)_5\cdot H_2O$ trigonal				
Gp Ap Cal	(i) Nodules (ii) Pseudomorph after bones	No data	Interaction between slightly acidic phosphatic solution and Ca-Al sediments	IL: Et-Tabun * [58] FR: Arago * [59] IT: Cocci and Carburangeli [24]
Variscite $Al(PO_4)\cdot 2H_2O$ orthorhombic				
Tar Lpp	Crusts, nodules and veinlets within the argillaceous material	No data	Interaction between acidic phosphatic solution and argillaceous matter	IL: Ornit * [1] RO: Cioclovina *, Gaura cu Muscă and Gaura Haiducească [60,61] MY: Batu, Gangub and Makangit [3]
Taranakite $(K,Na,NH_4)_3(Al,Fe^{3+})_5(HPO_4)_6(PO_4)_2\cdot 18H_2O)$ trigonal				
Lpp Var	Nodules in clay matrix	NH_4^+- and Fe^{3+}-bearing	Interaction between acidic phosphatic solution and argillaceous matter	IL: Ornit * [1] RO: Cioclovina *, Măgurici, Gura Dobrogei, Huda lui Papară, Gaura Haiducească, Gaura Muscă and Lazului [49,52,53,61–63] MY: Gangub and Makangit [3] IT: Eremita, Palombara, Corona'e sa Craba and Apulian Caves [24,46]
Leucophosphite $KFe^{3+}{}_2(PO_4)_2(OH)\cdot 2H_2O$ monoclinic				
Tar Var	Fine-grained crusts located at the center of guano layer enriched in clay material	Al^{3+}-bearing	Interaction between acidic phosphatic solution and Fe-rich siliciclastic matter	MY: Batu, Gangub and Makangit [3] IT: Corona 'e sa Craba [24] RO: Gaura cu Muscă and Lazului [61,63]

AU = Australia, ES = Spain, FR = France, IL = Israel, IT = Italy, MY = Malaysia, RO = Romania, SV = Salvador. * = archaeological cave sites Adl = ardealite, Ap = hydroxylapatite (carbonate-rich hydroxylapatite), Bsh = brushite, Bss = bassanite, Cal = calcite, Fan = francoanellite, Gp = gypsum, Lpp = leucophosphite, Tar = taranakite, Var = variscite. Main minerals are in bold.

The stage of strongly acidic pore waters in the deposits of caves that were abandoned long ago, including those at archeological sites, has finished in most cases. Authigenic phosphates in such caves are mostly Ca phosphates (apatite, brushite, etc.), which are stable in nearly neutral or slightly alkaline environments, thus indicating that the water–sediment system is approaching a steady state [1,45]. Denisova Cave is a bright example

of a different type, with a multilayer profile of various phosphates in the East Chamber (Figure 2d–f) [4].

4. Site Description

Sedimentary Sequence of East Chamber

Cave deposits in the Main and East Chambers at the Denisova site were described in terms of lithology and stratigraphy in previous publications [9,32,64]. The sedimentary sequence of the East Chamber comprises three main units separated by stratigraphic gaps. The basal unit lies on limestone bedrock (layer 17, ~2.5 m thick, correlated with layer 22 of the Main Chamber) and is composed of ochreous clay silt (loam) and heavy loam with limestone fragments bearing traces of dissolution (most often partially leached debris or, less often, boulders and blocks), with disseminated films of Fe-Mn (oxy)hydroxides. Their dendrites also cover pale-yellow bones of large mammals and small vertebrates. The sediment is interpreted as material redeposited in closed karst cavities [65–67]. Mean ages of sediments in layer 17 obtained from the Bayesian model correspond to Middle Pleistocene, bracketed between 508 ± 40 kyr and 284 ± 32 kyr BP [32].

The intermediate unit totals a thickness of 3.5 m and comprises layers 16 through 11, with sharp boundaries separated by stratigraphic gaps between layers 16 and 15, as well as between layers 14 and 13. Layer 16 consists of fine silt, and the 15–11 interval is dominated by light and medium clay silt, with sand or, occasionally, rubble in layers 13–15. Clay silt varies in color from brown to bright ochreous and reddish, and few intercalations are gray (layer 11.4). In general, the amount of clastic material (limestone debris and boulders) increases upward, from zero in layer 16 to few blocks of altered limestone in layer 13, and ≤30 vol. % clastics in layers 14 and 12.3, except for layer 15, with 40–50% of rounded blocks but ≥ 50% angular limestone fragments cemented with light clay silt in layers 12.2, 12.1, 11.4, 11.3, and 11.2 (Figure 3). The sediments host abundant coprolites and bones (detritus or well-preserved fragments) up to the top of layer 11 [65]. The unit was deposited after the karst cavity opened under environmental, biogenic, and anthropogenic effects [65]. According to paleoecological reconstructions [36,66], the deposition from the base of layer 15 at 203 ± 14 kyr to the top of layer 13 at 146 ± 11 kyr occurred in a warm and wet interglacial climate (MIS 7). The 12.3–12.2 interval (from 141 ± 10 kyr to 129 ± 11 kyr) corresponds to the cooling event of MIS 6; the interval from layer 12.1 to the base of layer 11.4 (from 120 ± 11 kyr to 105 ± 11 kyr) corresponds to the warm stage of MIS 5e; the interval between upper layer 11.4 and layer 11.3 (80 ± 9 kyr to 70 ± 8 kyr) was deposited during the cold stage of MIS 4; and the top of layer 11 (11.2 and 11.1; from 63 ± 6 kyr to 38 ± 9 kyr) formed in a relatively warm climate of MIS 3 [32].

The upper unit encompasses layers 9 to 6 and the overlying Holocene sediments, including anthropogenic layers 1–5, which are beyond this consideration. Layer 5 has an age of 4.5 cal kyr BP [30]. Phosphate mineralization occurs in layers 9–6, as well as in layers 11.1 and 11.2 (Figure 3).

Layer 9, (36 ± 4 kyr to 21 ± 8 kyr; Figure 3), which completes the Late Pleistocene stage of cave deposition in the East Chamber of Denisova Cave, formed during the coldest event of the last glacial maximum (LGM), corresponding to MIS 2 of marine oxygen stratigraphy. The layer is clearly separated from both layer 8 above and layer 11.1 below and varies in thickness from 20 to 30 cm. Digging in 2014 revealed a sharp boundary between layers 9 and 8, but the 10 cm deeper dig of 2016 exposed its later burrow disturbance. The base of layer 9 is uneven and follows the top of layer 11.1, with abundant limestone fragments currently replaced by Ca phosphates (Figures 2d–f, 3 and 4). Layer 9 (samples 8, 7, 6, 5) is composed of light-brownish silt, with the highest percentages of sand over the whole sampled sequence and abundant, dispersed ≤5 mm phosphate clots. The assemblage of phosphate minerals varies along the layer profile. Calcite is quite rare and is restricted to the cores of large limestone fragments mainly replaced by phosphates. The amount of phosphates is the lowest at sites abutting the cave walls; the sediment shows weak ebullition

with HCl, which reveals carbonate material (most likely fine limestone debris). The bone fragments found in the layer are decomposed to powder.

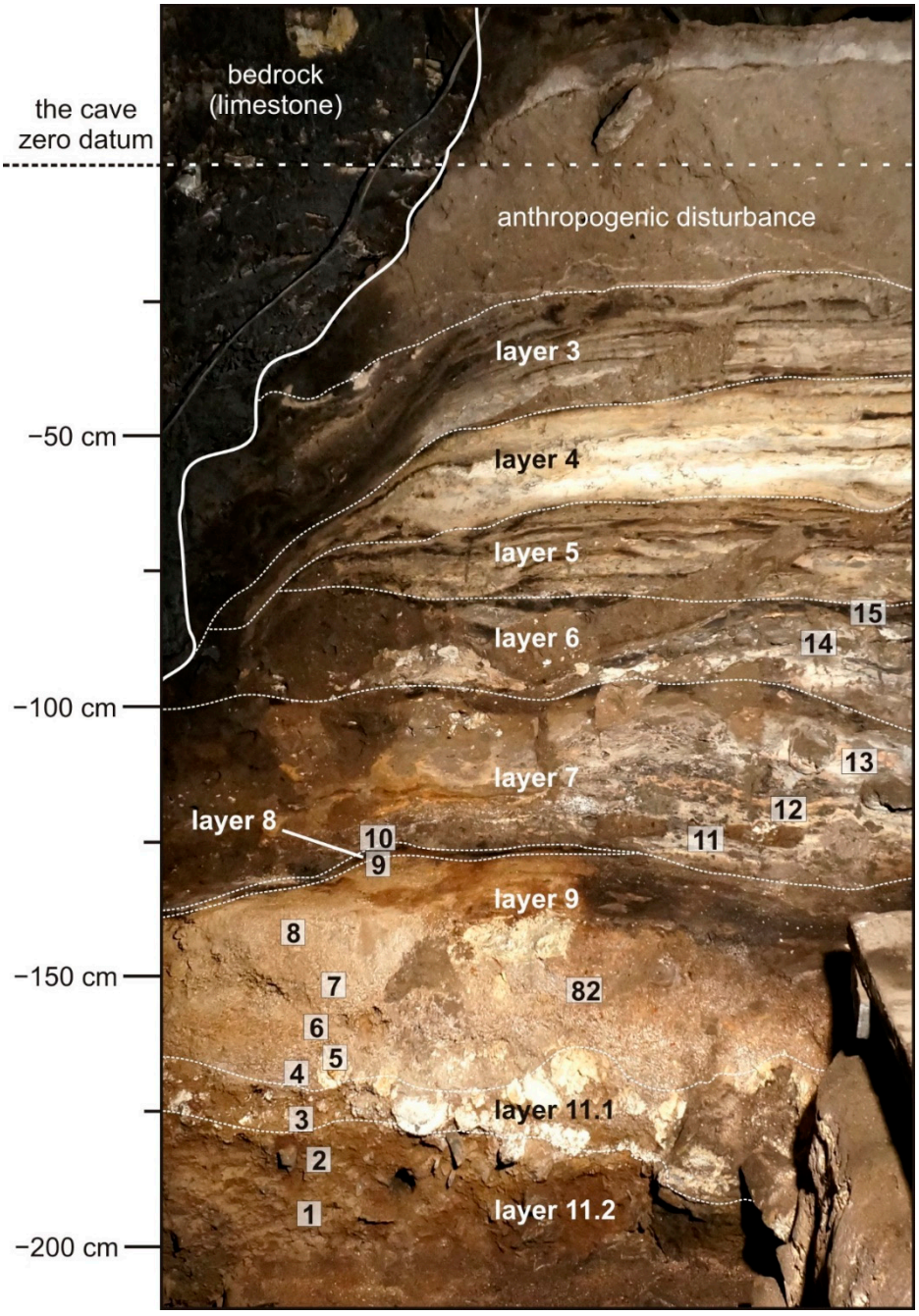

Figure 3. Phosphatic sedimentary sequence in the East Chamber of the Denisova Cave with sampling locations. The figures in white squares correspond to the sample numbers.

Figure 4. Stratigraphic sequence exposed in the East Chamber of Denisova Cave. (**a**) Photographs showing color and particle sizes of clay silt and silt in layers 6–11. Black sediments from layers 6 (sample 15) and 8 (sample 10) are especially rich in organic matter. Pale yellow to brown sediments of layer 9 are the richest in siliciclastic matter. Sediments of layer 11.1 contain large limestone fragments. Hereafter, samples are labeled as LX-SY, where X and Y are numbers of layers and samples, respectively. (**b**) Sampling sites.

Layer 8 (≤3 cm; Figures 3 and 4) comprises two subunits of different colors; the division is supported by the phase and major-element compositions of the sediments. The lower part, variable in thickness, is composed of brown silt with numerous whitish ≤1 cm nodules of quartz and feldspar particles tightly cemented with K-Al-Fe^{3+} phosphates (sample 9). The upper part consists of fine soft clay silt (sample 10) of brownish to black color, sooty and staining due to high contents of organic matter, the highest over the sampled sequence of the chamber (~28 wt% C_{org}), with numerous ≤2 mm and few ≤5–6 mm whitish and brownish nodules. Disseminated organic matter in the lower part of layer 8 coexists, with thin slices of N-rich organic matter and abundant well-preserved fragments of chitin partially replaced or encrusted with whitlockite and apatite on the surface. No ebullition under HCl was observed. The available ^{14}C ages of organic-rich sediments from

layer 8 (four determinations) are bracketed between 9495 ± 390 and 7700 ± 90, corresponding with the time of relatively warm climate conditions [30].

Layer 7 (Figures 3 and 4) is composed of light silt, mainly whitish and pale yellow in color, with some dark gray, reddish, or pinkish patches. The sediments are highly phosphatic and contain numerous phosphate nodules 0.3–1 cm in diameter. The layer base follows a black, sooty layer. Sediments at the base of layer 7 abound in Ca phosphate pseudomorphs after insect chitin. The primary sediments are heavily disturbed by burrows (≥50–60 vol%).

Layer 6 (Figures 3 and 4) is composed mainly of light clay silt of various colors, which does not react with HCl and lacks calcite according to XRD analysis. The sharp top and the base of the layer are delineated by 2–3 cm of black phosphate-rich, sooty material (sample 15 on the top). The base of the layer is overlain by mottled light clay silt with large, whitish phosphate patches in a pale yellow matrix. The layer is only 5–10 cm thick near the western wall of the chamber, where it is traceable only at the base, but is as thick as 20–25 cm in the center of the dig (Figure 3). The clay silt formerly enclosed abundant medium and fine limestone debris, but they have been almost fully replaced by Ca phosphates, which form thick reaction rims around limestone fragments and densely impregnate the space between them. The debris became rounded and lost the contours of individual fragments as a result of diagenetic alteration. The complex pattern of phosphate nodules formed by dissolution of primary limestones and precipitation of Ca phosphates. The layer bears signatures of heavy bioturbation (up to 50 vol% of burrows).

5. Materials and Methods

5.1. Sampling

Cave deposits in the East Chamber were sampled during the campaign of 2016 in the middle of the section excavated in 2014 by Dr. M. Kozlikin [68]. The sedimentary column is located at the entrance of the chamber, beneath the dome-shaped ceiling (Figure 2c,d), where the penetration of P-rich solutions as diagenetic agents was the deepest and most voluminous. The open section (profile) was sampled according to visible bedding based primarily on color difference of sediments (Figure 3). Authigenic phosphatic mineralization is traceable to a depth of 2 m below the cave datum. Eighteen samples were collected from the phosphatic sequence in Pleistocene-Holocene sediments of the East Chamber: soft sediments from 6–11.2 clay-sand-phosphate layers with clots, nodules, and aggregates of authigenic phosphate minerals; fragments of fresh and partly replaced limestone; and partly replaced paleolithic stone tools. The samples were dried at 30 °C and then kept in air- and water-tight plastic bags.

5.2. Analytical Procedures

The analytical work was carried out mainly at the Analytical Center for Multi-Elemental and Isotope Research (V.S. Sobolev Institute of Geology and Mineralogy (IGM), Novosibirsk, Russia) and at the South Ural Research Center of Mineralogy and Geoecology (SU FRC MG, Miass, Russia). Optical microscopy was combined with XRD and SEM/EDX analyses to study the phase composition and morphology of minerals, as well as the distribution of authigenic phosphate mineralization in different sediment layers from the East Chamber.

The samples for analysis were separated and purified under the binocular microscope by hand picking; some mineral aggregates were cleaned by weak ultrasonic treatment. Scanning electron microscopy (SEM) was applied to determine features of textures and morphology of minerals and their aggregates. The chemistry of minerals and amorphous phases was analyzed by SEM from energy-dispersive spectra (EDS), back-scattered electron (BSE) images, and elemental maps (EDS system) in fragments of sediments. All samples were coated with ~15 to 25 nm carbon films. Measurements were performed on a Tescan Mira 3MLU scanning electron microscope (Tescan Orsay Holding, Brno, Czech

Republic) equipped with an Oxford Aztec Energy Xmax-50 microanalysis system (Oxford Instruments Nanoanalysis, Abingdon, UK) at IGM (Novosibirsk). An accelerating voltage of 20 kV and a 1 nA beam current were used in high-vacuum modes for a 20 s count time.

X-ray diffraction (XRD) analysis was applied to bulk sediment samples and separate mineral fractions. Mineral phases (≥1%) were identified by XRD in powdered samples. Measurements were performed on a Shimadzu XRD-600 diffractometer (Shimadzu Corporation, Kyoto, Japan) (Cu$K\alpha$ radiation with a graphite monochromator, λ = 1.54178 Å) at SU FRC MG (Miass). The scans were recorded from 6 to 60°2θ at 0.05°2θ increments with a 5 s scanning time per step. SIROQUANT V.4 software was used to calculate the proportions of minerals. For analytical details, see [69].

Major elements in bulk sediment samples were analyzed by the ICP-AES technique (inductively coupled plasma atomic emission spectroscopy) on a ThermoJarrell IRIS Advantage atomic emission spectrometer (ThermoJarrell Intertech Corporation, Atkinson, WI, USA) at IGM (Novosibirsk). The preconditioning procedure included fusion of powdered whole-rock samples with lithium borate [70].

C-H-N-S analyses of organic matter were carried out at the N.N. Vorozhtsov Novosibirsk Institute of Organic Chemistry SB RAS (Novosibirsk) using *Hewlett-Packard model 185* (United States) and *Euro EA 3000* (Italy) analyzers.

6. Results

6.1. Bulk Rock Chemistry

Phosphates occur in soft sediments as abundant, light-colored (to whitish), closely packed nodules and intergrowths (fractions of mm to 1.5 cm) (Figure 4). The sediment color varies from brownish or gray to pale yellow (taupe), depending on the percentages of phosphates. Thin black layers appear at three levels in the sedimentary sequence: at the top of layers 6 and 7 and in the interval of layer 8 and the top of layer 9 (taupe sample 8). The black layers contain remnants of chitin particles (Figure 5) and/or biofilms of N-rich organic matter. Chitin particles were also present in primary sediments and throughout layer 7 (samples 11, 12, 13), where they are currently converted into Ca phosphate pseudomorphs.

The major-element profile in the open section has a complex pattern, but the element contents vary concordantly in several intervals (Figure 6). The thin black layers (samples 15 and 10) have similar and very particular chemical signatures, with the highest loss on ignition (LOI; about 29 and 50 wt%, respectively), mainly due to organic matter. Both these layers also have the lowest contents of elements associated with the siliciclastic component of the cave sediments (SiO_2, TiO_2, Al_2O_3, Fe_2O_3, Na_2O, and K_2O) (Figure 6, Tables 2 and 3). Both CaO and P_2O_5 in sediments from layer 6 approach the maximum contents (29.22 and 32.31 wt%, respectively). The sediments of layer 7 differ in the highest concentrations of Ca, Mg, P, and S at moderate LOI. Sediments from layer 9 are the richest in siliciclastic matter (except for the layer base, sample 4), judging by the concordant increase in SiO_2, TiO_2, Al_2O_3, Fe_2O_3, Na_2O, and K_2O to the highest levels, whereas MnO, MgO, CaO, and SO_3 decrease abruptly.

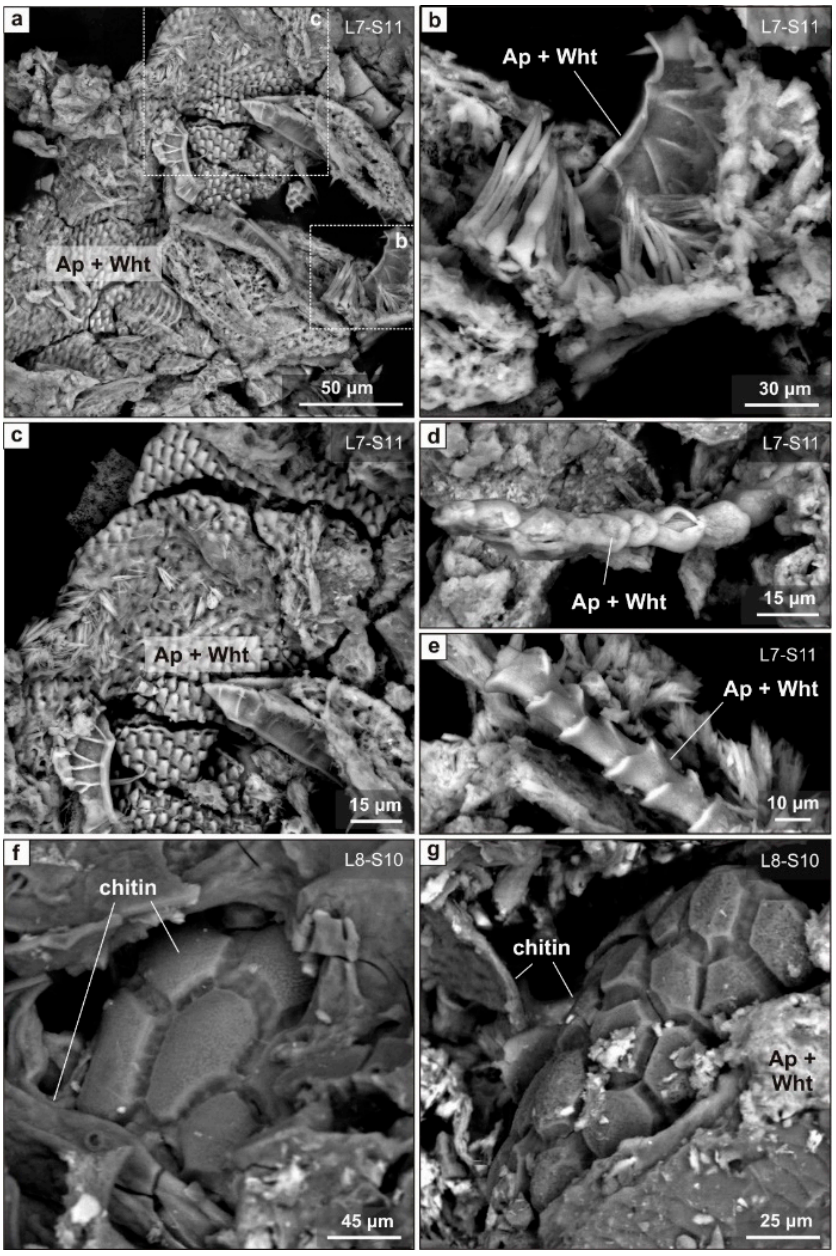

Figure 5. Back-scattered electron (BSE) images of insect remains from the East Chamber of Denisova Cave. (**a**–**e**) Ca and Ca-Mg phosphate (hydroxylapatite and whitlockite) pseudomorphs after fragments of insect exoskeletons. (**f,g**) Well-preserved insect remains not replaced by phosphates. Ap = apatite, Wht = whitlockite.

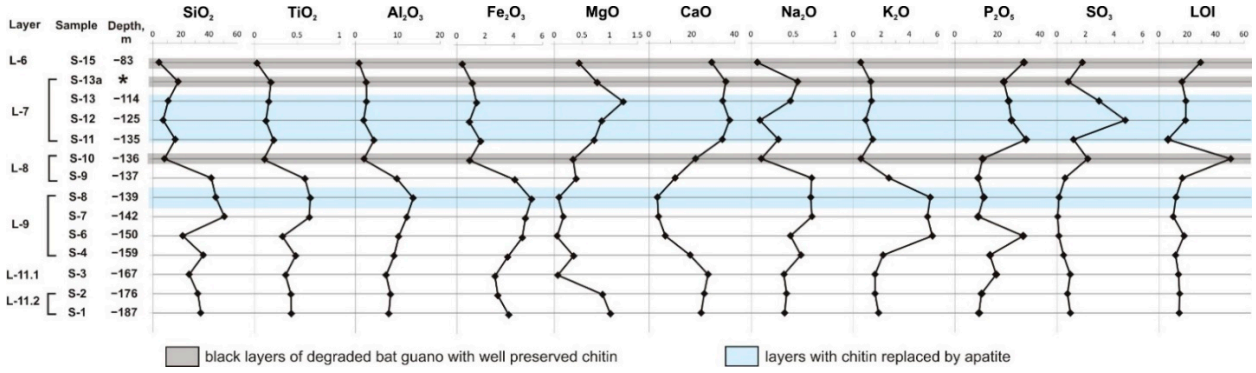

Figure 6. Major-element contents (wt%) in sediments with authigenic phosphate mineralization from the East Chamber of Denisova Cave. Element contents are presented in Table 2. * Sample S-

13a is from the South Chamber of Denisova Cave, from a stratigraphic equivalent of the top of layer 9 in the East Chamber, where the corresponding interval was eliminated by burrowers.

Table 2. Major-element compositions of sediments with authigenic phosphate mineralization from the East Chamber of Denisova Cave (northwest Altai) (wt%).

Layer	Sample	SiO_2	TiO_2	Al_2O_3	Fe_2O_3	MnO	MgO	CaO	Na_2O	K_2O	P_2O_5	SO_3	ZnO	CuO	Total
L-6	S-15	4.34	0.03	0.87	0.39	0.09	0.44	29.22	0.07	0.51	32.31	1.77	0.57	0.05	99.97
L-7	S-13a	17.91	0.19	2.57	1.08	0.08	0.77	35.84	0.55	1.23	22.91	0.78	0.10	0.05	100.23
L-7	S-13	10.81	0.16	2.62	1.38	0.09	1.24	34.37	0.47	1.28	25.15	2.93	0.36	0.06	99.92
L-7	S-12	7.28	0.13	1.91	0.88	0.05	0.85	37.55	0.10	0.87	26.53	4.76	0.27	0.07	99.96
L-7	S-11	15.83	0.22	4.38	1.67	0.05	0.72	34.23	0.32	1.37	33.27	1.14	0.33	0.04	99.96
L-8	S-10	8.17	0.11	1.93	0.89	0.02	0.34	21.66	0.12	0.53	12.94	2.14	0.36	0.18	99.89
L-8	S-9	41.45	0.59	9.82	4.07	0.15	0.39	12.12	0.72	2.53	10.92	0.55	0.12	<0.02	99.91
L-9	S-8	44.64	0.65	13.63	5.23	0.01	0.07	3.85	0.70	5.47	13.49	0.14	0.09	<0.02	99.97
L-9	S-7	50.74	0.64	12.12	4.81	0.03	0.16	4.38	0.72	5.28	10.89	0.05	0.08	0.02	100.00
L-9	S-6	21.20	0.33	10.21	4.59	0.03	0.05	7.57	0.47	5.62	31.99	0.13	0.09	<0.02	99.98
L-9	S-4	35.75	0.48	9.13	3.56	0.18	0.35	19.13	0.59	2.10	16.41	0.45	0.08	<0.02	99.96
L-11.1	S-3	25.71	0.36	7.26	2.67	0.14	0.06	27.55	0.39	1.54	19.32	0.92	0.03	<0.02	99.74
L-11.2	S-2	31.87	0.43	8.30	2.88	0.08	0.87	25.77	0.42	1.54	12.49	0.73	0.04	<0.02	99.96
L-11.2	S-1	33.96	0.43	7.88	3.64	0.06	1.01	24.29	0.40	1.79	11.29	0.92	0.05	<0.02	99.97

All iron is calculated as Fe_2O_3. LOI = loss on ignition.

Table 3. Contents of C_{org}, H, N, and S_{org} in sediments with authigenic phosphate mineralization from the East Chamber of Denisova Cave (northwest Altai) (wt%).

Layer	Sample	C_{org}	H	N	S
L-6	S-15	7.68	1.34	2.17	2.86
L-7	S-13a	3.39	0.97	0.49	<0.3
L-7	S-13	<0.3	1.20	<0.3	3.44
L-7	S-12	0.69	1.17	<0.3	3.48
L-7	S-11	0.81	0.45	0.33	0.44
L-8	S-10	27.84	1.90	7.88	0.39
L-8	S-9	4.77	0.97	0.95	<0.3
L-9	S-8	1.07	1.07	<0.3	<0.3
L-9	S-7	1.09	0.85	<0.3	<0.3
L-9	S-6	1.74	1.51	0.37	<0.3
L-9	S-4	1.83	0.88	0.42	<0.3

The major-element chemistry of bulk sediments is affected by the presence of abundant limestone boulders at the base of the sedimentary sequence (layer 11, samples 1–3). The contents of Ca and Mg, as well as S, which were originally related to Mg-bearing calcite and pyrite in the limestone, increase gradually on transition from layer 9 to layer 11. The contents of SiO_2, TiO_2, Al_2O_3, Na_2O, and K_2O are moderate and stable throughout the sampled interval of layer 11 and record the amount of siliciclastic matter.

The depth profiles of main siliciclastic minerals (quartz, plagioclase, and mica) in layers 6–11 of the East Chamber are similar and generally correspond to Si, Ti, Al, and Fe profiles. Feldspar is present in notable amounts only in layers 9 and 11 (5–7% and 4%, respectively). Calcite was identified by XRD analyses only in samples from layer 11, and its percentage increases with depth (1 to 14 % in 20 cm interval) in inverse proportion to phosphorus contents in sediments of the same layer (Figure 7).

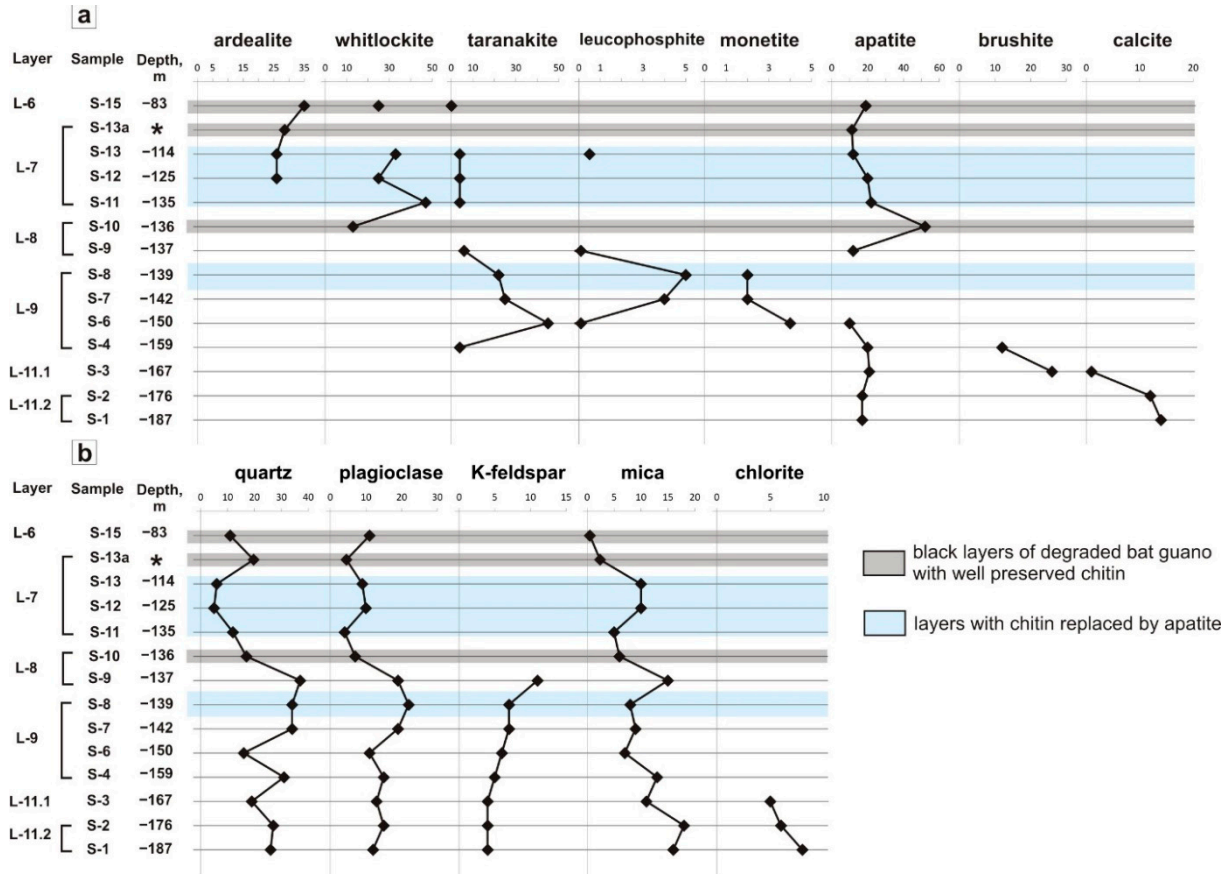

Figure 7. Percentages of authigenic phosphates (**a**) and siliciclastic minerals (**b**) in cave sediments from the East Chamber of Denisova Cave. XRD data, wt%.

6.2. Depth Profiles of Phosphate Minerals in the East Chamber

Authigenic phosphates in the sedimentary sequence of the East Chamber show distinct vertical zoning. Their assemblages become generally less diverse with depth, from five minerals in layers 6–7 to one or two minerals in layer 11; the total content of phosphates in the bulk sediments decreases from 79% (sample 15) to 17% (sample 1–2). Ardealite and whitlockite are main P-bearing phases only in the upper part of the excavated sequence (layers 6 and 7); ardealite decreases with depth from 35 to 26 % and disappears in the middle of layer 7 below −125 cm, whereas whitlockite reaches deeper depths (−136 cm, top of layer 8), representing the most abundant phase (up to 47%) in layer 7 (Figure 7). Apatite (12–22%) and taranakite (≤4%) are ubiquitous in layers 6 and 7, whereas leucophosphite is restricted to a few micrograins (sample 13) in the top of layer 7.

Sediments at the base of layer 7 (sample 11) and thin layer 8 (samples 9,10) contain an assemblage of phosphates less diverse than in those of the previous interval, with predominant apatite (up to 52%), no ardealite, whitlockite decreasing from 13% to 0%, and only sporadic taranakite and leucophosphite.

The mineralogy of phosphates changes dramatically in layer 9; K-Al (22–45% taranakite) and K-Fe^{3+} (up to 5% leucophosphite) phosphates supersede apatite and whitlockite, which were predominant in layers 6–8. Samples with low (10%) or absent apatite bear a rare phosphate of monetite (2–4%), which contains 14 wt% less CaO than apatite.

Another dramatic change in phosphate mineralogy occurs at the boundary of layers 9 and 11, where the assemblage becomes bimineral, comprising apatite (~20%) and brushite (12–26%) within a narrow interval from −159 to −167 cm; then, apatite (17%) becomes the only phosphate at the base of layer 11.2, and the amount of calcite increases.

6.3. Distribution of Phosphate Assemblages by Layer

Layer 6, 20–25 cm: soft clay silt of various color nuances; black, sooty material with fatty luster from the top of layer 6 (sample 15) containing numerous small (≤3 mm) light gray phosphate nodules; mainly amorphous N-rich organic matter (C_{org} ~ 7.7 wt% and N ~ 2.2 wt%) and phosphates (79% of the total amount of crystalline phases) at low percentages of siliciclastic matter (11% of quartz and plagioclase each) (Figure 7); preserved chitin fragments; phosphates appear as solid cavernous aggregates of grains, with predominant ardealite or Ca and Ca-Mg phosphates, mainly whitlockite and apatite (Figure 8).

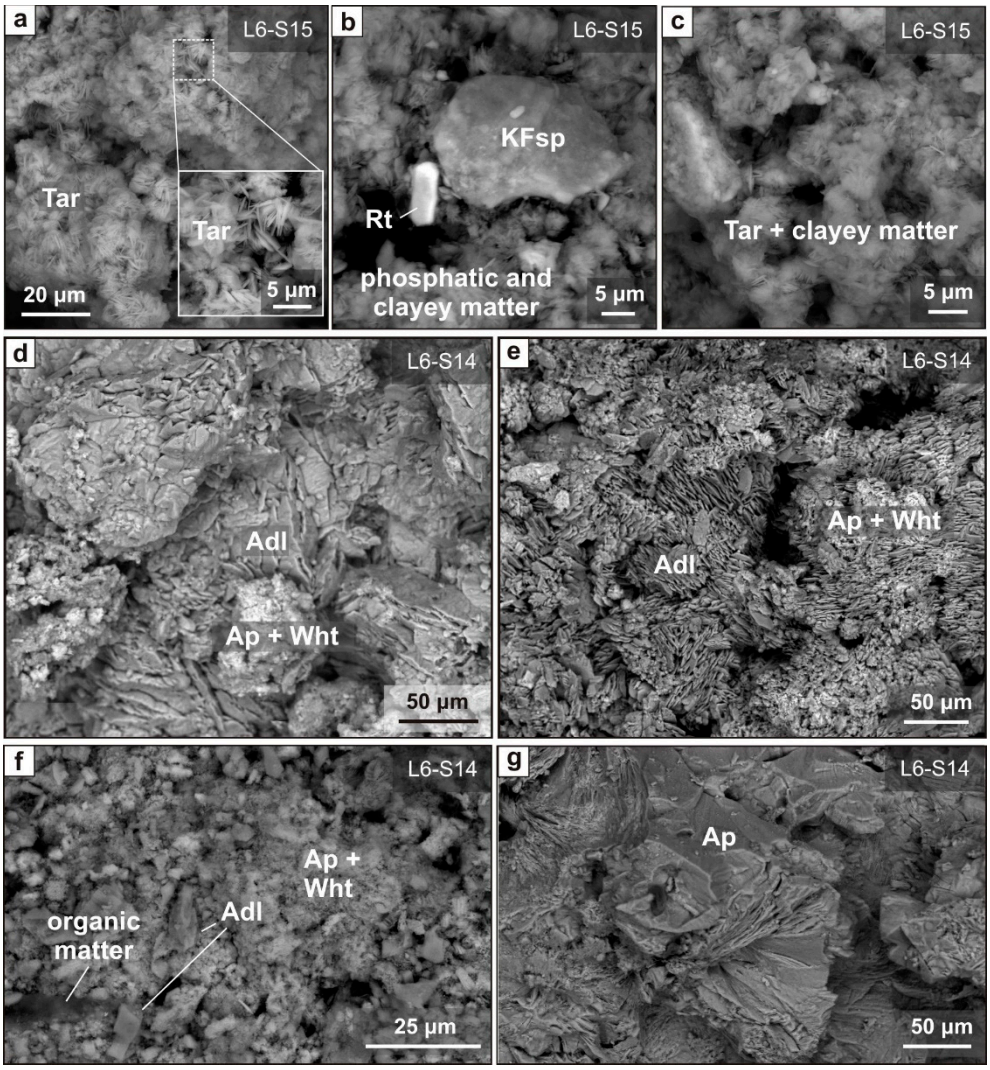

Figure 8. Back-scattered electron (BSE) images showing the diversity of phosphates from layer 6, East Chamber of Denisova Cave. (**a**) Nodular taranakite aggregate: rose-like intergrowths of typical platy grains. (**b**) Rutile and altered potassium feldspar in a matrix of phosphatized clayey matter. (**c**) Fine-grained aggregate of newly formed taranakite cementing clayey matter. (**d**,**e**) Quasi-parallel intergrowths of flat ardealite crystals with dusty apatite and whitlockite in the interstitial space. (**f**) Fine ardealite crystals buried in fine-grained matrix of apatite and whitlockite. (**g**) An aggregate of coarse anhedral apatite crystals. Adl = ardealite, Ap = apatite, KFsp = potassium feldspar, Rt = rutile, Tar = taranakite.

Ardealite occurs as a regular aggregate of quasi-parallel, envelope-like, flat 60–100 µm euhedral crystals (Figures 8e and 9a) of several generations that formed in different episodes of nucleation and growth, some with signatures of dissolution. Ca and Ca-Mg phosphates in such aggregates commonly appear as a fine, dusty mixture in the interstitial space or on the surfaces of ardealite (Figure 8d,e,f). In the absence of ardealite, apatite and

whitlockite make up dense aggregates of 100–150 μm anhedral or subhedral grains (Figure 8g).

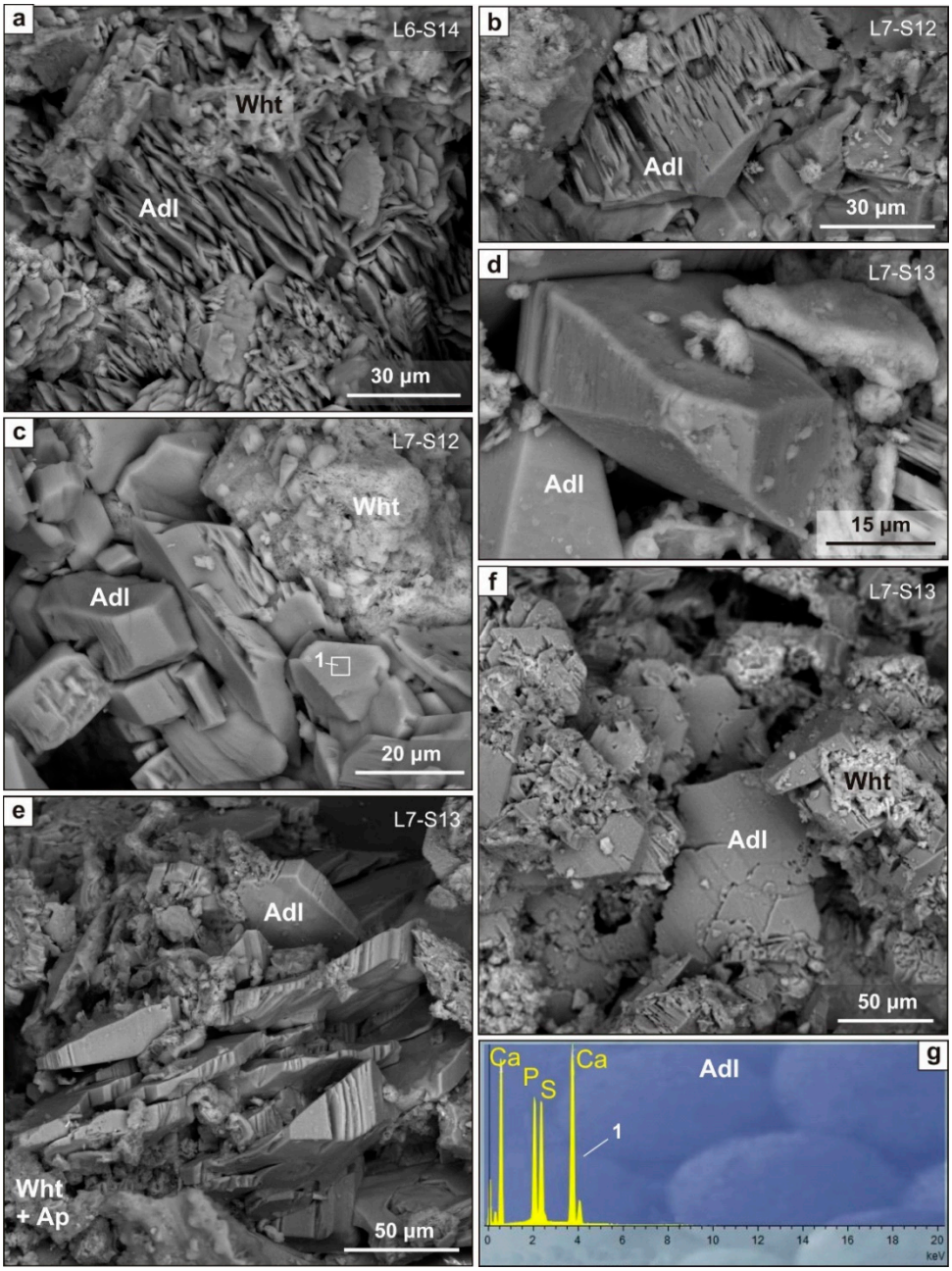

Figure 9. Back-scattered electron (BSE) images showing the morphology and typical EDS spectrum of ardealite, East Chamber of Denisova Cave. (**a**) Quasi-parallel intergrowths of flat (envelope-shaped) ardealite crystals with fine-grained whitlockite in the interstitial space. (**b**–**d**) Prismatic ardealite crystals elongate along the *b* axis with prominent (**b**,**c**) and poorly pronounced (**d**) etching relief on the faces of ardealite. (**e**) Prismatic ardealite crystals with fine-grained whitlockite and apatite in the interstitial space. (**f**) Hopper-like crystals of ardealite growing over fine-grained whitlockite; (**g**) typical EDS spectrum of ardealite (in keV). Adl = ardealite, Ap = apatite, Wht = whitlockite.

Taranakite occurs as up to 300 μm nodules composed of numerous rose-like intergrowths, each an aggregate of ≤10 μm platelets (Figures 8a–c and 10a). SEM-EDS analyses of taranakite from this layer reveal up to 2–4 wt% N, but it remains unclear whether it is incorporated into taranakite structure as $(NH_4)^+$-groups via restricted substitution $K^+ \rightarrow (NH_4)^+$ or inherited from N-rich organic matter (OM) disseminated in the mineral matrix.

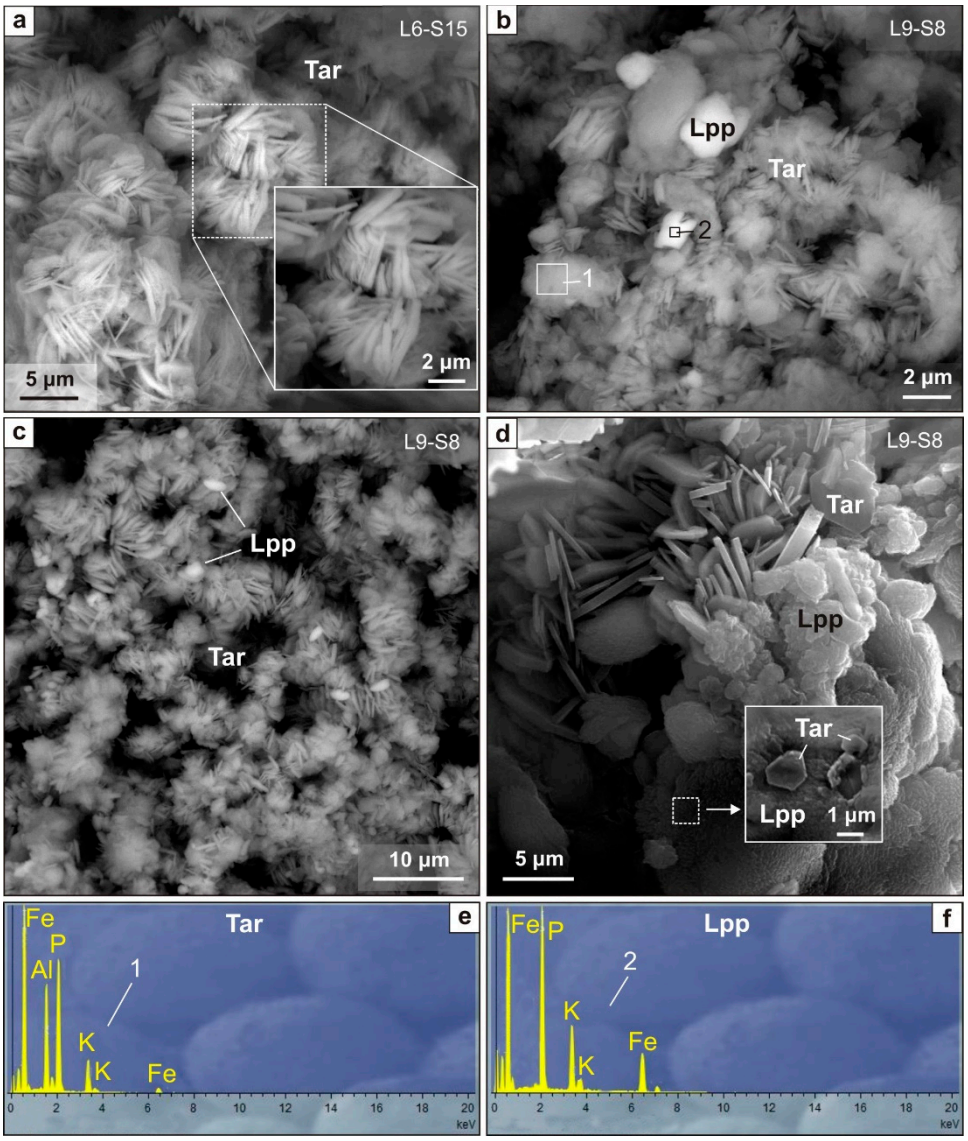

Figure 10. Back-scattered electron (BSE) (**a**–**c**) and secondary electron (SE) (**d**) images showing the morphology and typical EDS spectra of taranakite and leucophosphite, East Chamber of Denisova Cave. (**a**) Nodular taranakite aggregate: euhedral platy to tabular grains. (**b**,**c**) Aggregates of platy taranakite crystals and individual round (**b**) and rice-like (**c**) leucophosphite clots. (**d**) Rose-like intergrowths of tabular early taranakite covered by fine-grained leucophosphite aggregates, with hexagonal platy late taranakite on surfaces of leucophosphite. (**e**) Typical EDS spectrum of taranakite (in keV). (**f**) Typical EDS spectrum of leucophosphite (in keV). Lpp = leucophosphite, Tar = taranakite.

Layer 7 (samples 13, 12, and 11 from the top, middle, and base of the layer, respectively), 30–35 cm thick: soft brownish sediments with numerous phosphate nodules, 0.3–1 cm in diameter. Phosphate assemblages are similar on the top and in the middle of the layer, with abundant ardealite and whitlockite, less abundant apatite, and ubiquitous taranakite (4 %); trace amounts of leucophosphite are restricted to the top of the layer (Figures 7 and 11). At the layer base, ardealite disappears, whitlockite reaches its maximum over the sequence (47%), and apatite forms numerous pseudomorphs after chitin particles (Figure 12a).

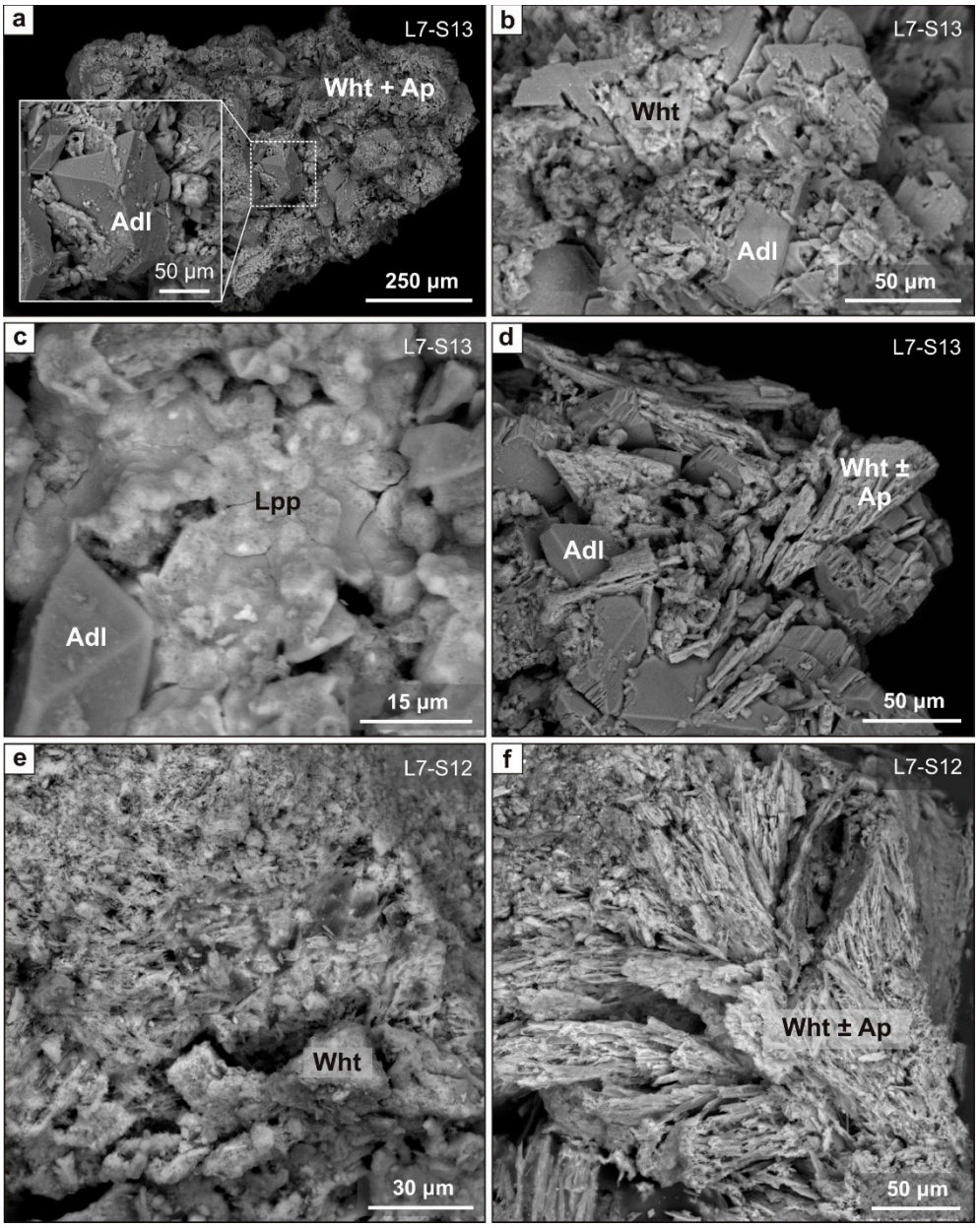

Figure 11. Back-scattered electron (BSE) images showing the diversity of phosphates from layer 7 (top and middle), East Chamber of Denisova Cave. (**a**) Pseudoprismatic ardealite crystals buried in fine-grained whitlockite matrix. (**b**) Hopper ardealite crystals growing over fine-grained whitlockite. (**c**) Euhedral ardealite crystals cemented by earthy-looking leucophosphite aggregate. (**d**) Aggregate of ardealite crystals and fan-shaped whitlockite. Apatite occurs as a minor phase. (**e**) Aggregate of randomly oriented fine whitlockite. (**f**) Fan-shaped aggregate of whitlockite and apatite. Adl = ardealite, Ap = apatite, Lpp = leucophosphite, Tar = taranakite, Wht = whitlockite.

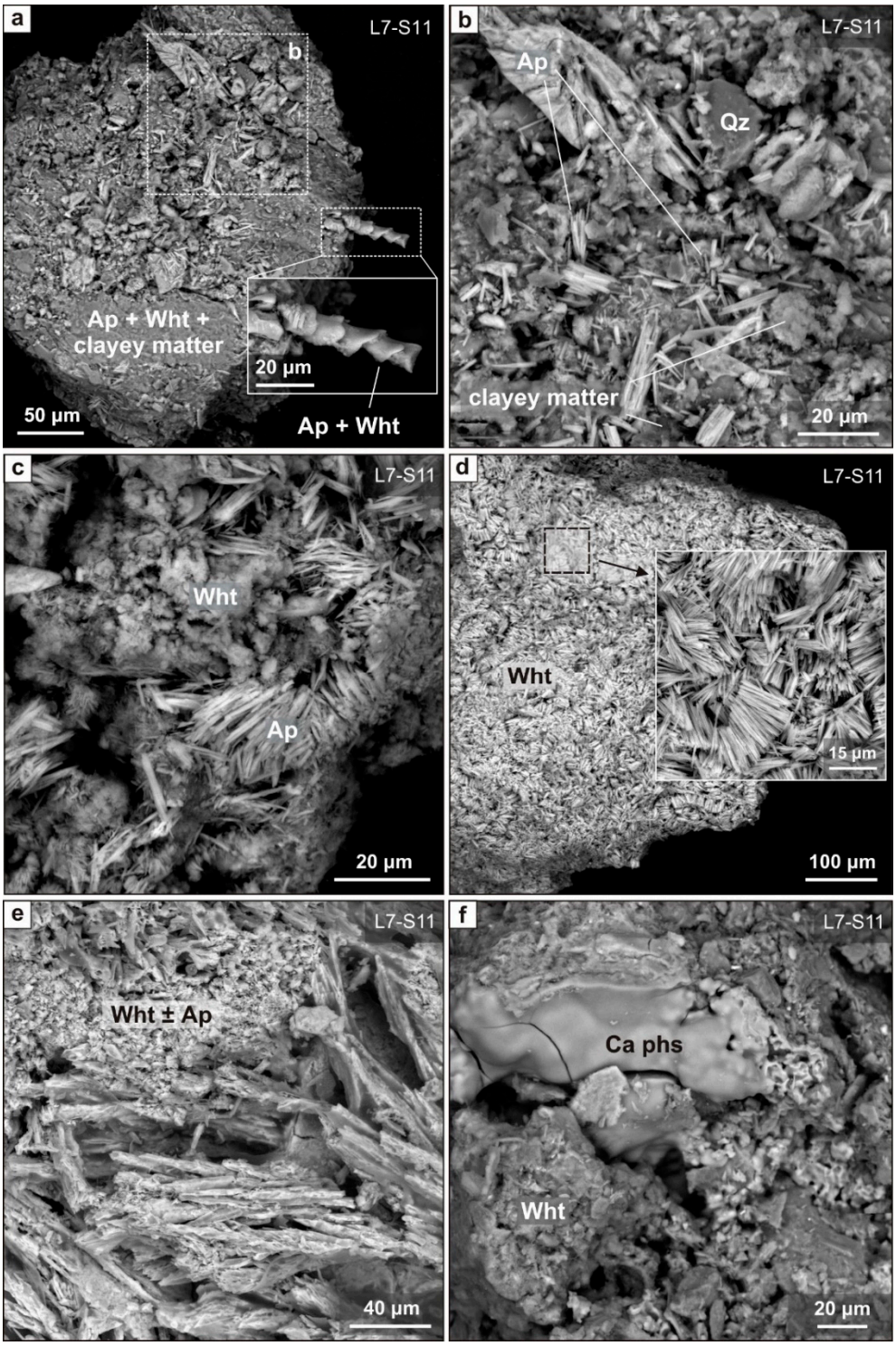

Figure 12. Back-scattered electron (BSE) images showing the diversity of phosphates from layer 7 (bottom), East Chamber of Denisova Cave. (**a**) Pseudomorphs of Ca and Ca-Mg phosphates (apatite and whitlockite) after a fragment of insect antenna or leg (?) in a clayey matrix. (**b**) Randomly oriented elongate apatite in a siliciclastic matrix. (**c**) Aggregate of powdery whitlockite and bladed apatite. (**d**) Irregular aggregate of thin elongated to needle-like whitlockite of different sizes. (**e**) Aggregate of fan-shaped whitlockite and apatite. (**f**) Rare botryoidal aggregates of Ca phosphates coating the surface of a fine-grained whitlockite aggregate. Ap = apatite, Ca phs = Ca phosphates, Qz = quartz, Wht = whitlockite.

Ardealite occurs as 20–100 μm euhedral crystals of various habits or their aggregates (Figure 9b–f). The crystals are most often prismatic (epidote morphological type) and

elongated along the b axis, with prismatic and pinacoidal faces, mainly {110} and {100} (Figure 9c,d,e). Many crystals are envelope-shaped (titanite morphological type), and some are platy (Figure 9a). Dissolution signatures are often present on faces or, less often, on edges (Figure 9b–d), especially in ardealite from the middle part of the layer (sample 12). Ardealite from the top of the layer is often in the form of hopper-like crystals growing over the cores of fine whitlockite aggregates (Figures 9f and 11b). Coarse ardealite is commonly intergrown with fine or, less often, prismatic or platy whitlockite crystals (Figure 11d). Some ardealite crystals are cemented with massive fine leucophosphite (Figure 11c). Coarse, flat ardealite grains are suitable for SEM-EDS analysis (Table 4 and Figure 9g), and show a nearly stoichiometric mineral chemistry typical of cave environments [51,52,57,71].

Table 4. Representative EDS compositions (wt%) of taranakite, brushite, ardealite, and whitlockite from the East Chamber of Denisova Cave.

Phase	Taranakite $(K,Na,NH_4)_3(Al,Fe^{3+})_5(HPO_4)_6(PO_4)_2{\cdot}18H_2O$				Brushite $Ca(HPO_4){\cdot}2H_2O$				Ardealite $Ca_2(SO_4)(HPO_4){\cdot}4H_2O$				Whitlockite $Ca_9(Mg,Fe^{2+})(PO_4)_6(HPO_4)$			
			Layer 9				Layer 11.1				Layer 7				Layer 7	
Sample	Theor.	1	S-8	S-8	Theor.	2	S-82	S-82	Theor.	3	S-12	S-12	Theor.	4	S-12 *	S-11 **
K_2O	10.53	7.09	7.6	8.9		n.a.	<0.3	<0.3		n.a.	<0.3	<0.3		n.a.	0.3	2.1
Al_2O_3	18.99	19.03	20.8	21.6		n.a.	<0.3	<0.3		n.a.	<0.3	<0.3		0.22	<0.3	<0.3
Fe_2O_3		0.42	1.5	1.6		n.a.	<0.3	<0.3		n.a.	<0.3	<0.3		n.a.	<0.3	<0.3
CaO		n.a.	0.7	0.7	41.24	40.53	42.7	41.8	32.58	31.14	31.4	31.3	47.05	46.16	45.3	46.8
SrO		n.a.	1.4	1.6		n.a.	0.9	0.8		n.a.	<0.3	<0.3		0.44	1.4	0.6
MgO		n.a.	<0.3	<0.3		n.a.	<0.3	<0.3		n.a.	<0.3	<0.3	2.52	2.03	2.3	1.2
FeO		n.a.	<0.3	<0.3		n.a.	<0.3	<0.3		n.a.	<0.3	<0.3	3.23	2.32	0.9	0.4
Na_2O		n.a.	<0.3	<0.3		n.a.	<0.3	<0.3		n.a.	<0.3	<0.3		0.80	0.5	<0.3
CuO		n.a.	<0.3	<0.3		n.a.	<0.3	<0.3		n.a.	<0.3	<0.3		n.a.	0.4	<0.3
ZnO		n.a.	<0.3	<0.3		n.a.	<0.3	<0.3		n.a.	<0.3	<0.3		n.a.	0.5	<0.3
P_2O_5	42.30	42.32	41.0	40.7	32.59	32.12	32.7	31.4	20.62	21.31	20.7	21.5	46.35	47.17	44.5	47.9
SO_3		n.a.	<0.3	<0.3		n.a.	1.2	0.9	23.26	22.75	23.2	22.8		n.a.	2.5	<0.3
H_2O	28.18	31.10	n.a.	n.a.	26.17	26.39	n.a.	n.a.	23.55	24.86	n.a.	n.a.	0.84	0.82	n.a.	n.a.
Total	100.00	99.96	73.0	75.1	100.00	99.04	77.5	74.9	100.00	100.06	75.3	75.6	100.00	99.96	98.3	99.0

Samples S-8, S-82, S-11, and S-12 = cave sediments from the East Chamber of Denisova Cave. Whitlockite from Denisova Cave: * = fan-shaped, ** = thin elongated to needle-like, theor. = theoretical composition, n.a. = not analyzed, 1 = taranakite from Onio-Iwaya Cave, Japan [72], 2 = brushite from Apulian Caves, Italy [46], 3 = ardealite from La Guandola Cave, Italy [71], 4 = whitlockite from Palermo Mine [73].

Whitlockite, another main phosphate phase besides ardealite, reaches 47 % at the base of the layer (sample 11) (Figures 7 and 11–13) and often appears as prismatic and platy grains intergrown with apatite (Figures 11f and 12c,e). Fine porous aggregates of whitlockite overgrown with ardealite hopper-like crystals were also found in sediments from the top of the layer (Figures 11b and 13d). Sediments in the middle of the layer contain abundant, fine-grained apatite–whitlockite intergrowths where individual phases and grains are hard to identify (Figure 11e). Such mixes include main components of Ca, Mg, Fe, and P, as well as impurities of Na, Zn, Cl, and S. Ca and Ca-Mg phosphates often occur as full pseudomorphs after chitin particles that are remarkably by preserved micromorphology of insect exoskeletons (Figures 5a–e and 12a). Taranakite was identified only by XRD analyses.

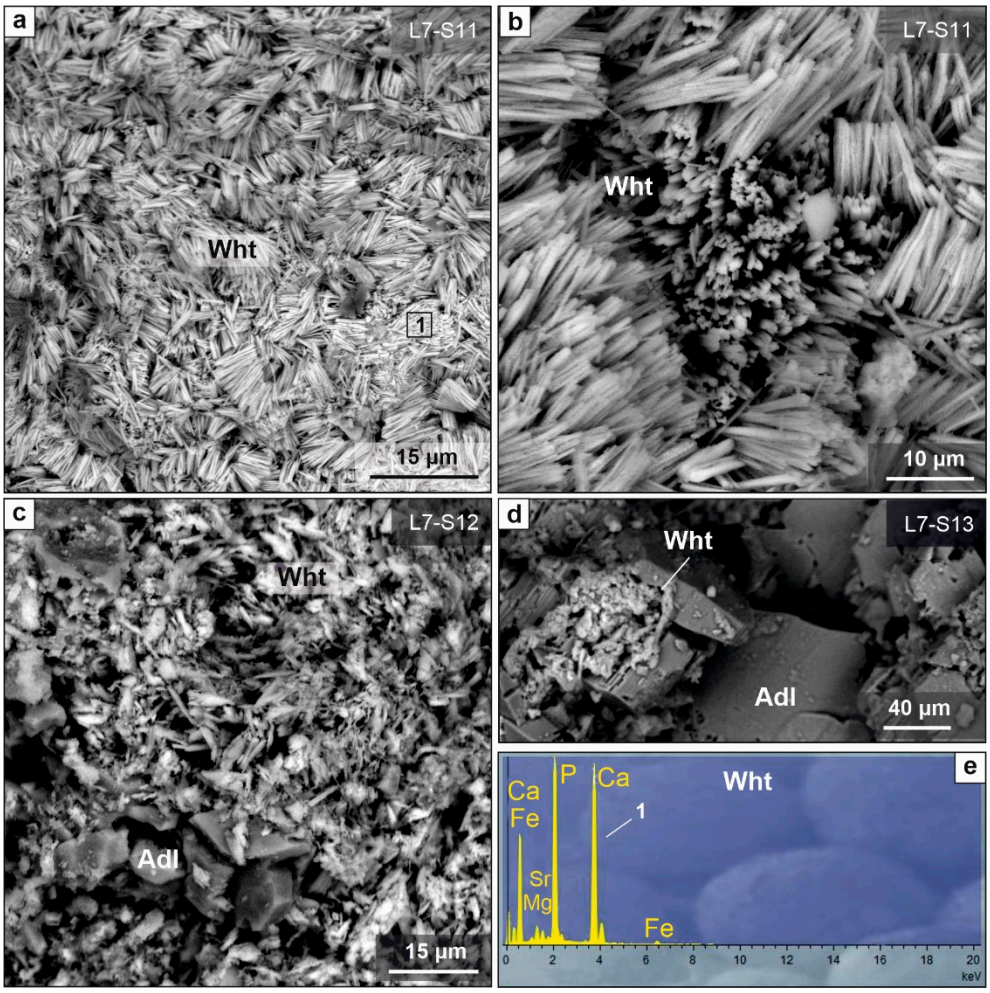

Figure 13. Back-scattered electron (BSE) images showing the morphology and typical EDS spectra of whitlockite, East Chamber of Denisova Cave. (**a**,**b**) Closely packed bunches of quasi-parallel needle-like whitlockite. (**c**) Aggregate of randomly oriented whitlockite microcrystals in the interstitial space between ardealite crystals. (**d**) Hopper crystal of ardealite growing over microgranular whitlockite aggregate. (**e**) Typical EDS spectrum of whitlockite (in keV). Adl = ardealite, Wht = whitlockite.

In all layers with partially degraded OM, whitlockite occurs as vuggy aggregates of coarse prismatic angular crystals (Figures 11d–f and 12e) and has particularly reproducible chemistry (Table 4). Such whitlockite has the greatest MgO enrichment (1.5–3.5 wt%; $X_{av.}$= 2.5 wt%) and contains notable amounts of Na_2O (0.5–0.8 wt%; $X_{av.}$= 0.6 wt%), SrO (0.7–1.5 wt%; $X_{av.}$= 1.1 wt%), FeO (0.4–1.6 wt%; $X_{av.}$= 0.8 wt%), SO_3 (1.6–3.8 wt%; $X_{av.}$= 2.2 wt%), and ZnO (0.5–0.8 wt%; $X_{av.}$= 0.6 wt%). They differ from the stoichiometric composition of $Ca_9(Mg,Fe)(PO_4)_6(HPO_4)$ in lower percentages of both main components CaO (41.9–46.1 wt%; $X_{av.}$= 44.5 wt% vs. 47.1 wt%) and P_2O_5 (43.9–46.6 wt%; $X_{av.}$= 44.5 wt% vs. 46.4 wt%) (Table 4). Whitlockite pseudomorphs after chitin particles contain up to 0.4 wt% CuO. The XRD pattern of coarse prismatic whitlockite is identical to that of $HCa_9Mg(PO_4)_7$ (04–009-3397; data base PDF-4+ (2009) [74].

At the boundary between layers 7 and 8, whitlockite occurs as morphologically and compositionally different monomineral aggregates of bunched, thin, and relatively short (~10–12 μm) prisms. The bunches are randomly oriented relative to one another, but individual grains remain quasi-parallel within each bunch (Figures 12d and 13a,b). The mineral chemistry is more homogeneous in this case, but there are few reliable analyses (n = 5). As to average element contents, whtilockites of this type are higher in CaO (46.4 wt%), P_2O_5 (46.6 wt%), and K_2O (2.1 wt%) but lower in MgO (1.1 wt%), FeO (0.4 wt%), and SrO (0.6 wt%). The contents of ZnO and SO_3 are below the detection limits (< 0.3 wt%) (Table

4). The XRD pattern of this whitlockite of high crystallinity is identical to that of Ca-rich synthetic whitlockite ($HCa_{2.89}Mg_{0.11}(PO_4)_2$; 04-010-2971 database PDF-4+ (2009) [74]). Whitlockite of another type with a more prefect structure and lower contents of impurities likely results from recrystallization of earlier compositionally complex coarse prismatic whitlockite.

Layer 8 contains a black layer with abundant, well-preserved chitin fragments and particles of organic matter on the top (Figures 5f,g and 14a,b), with 5–9 wt% N in biogenic compounds and relatively low percentages of siliciclastic material (30% vs. 82% at the layer base). Apatite spikes to its highest percentage over the profile (up to 52 %), and aggregates of coarse prismatic apatite occur on the surfaces and between chitin and organic particles (Figure 14a). The same aggregates often contain relatively low percentages of whitlockite; this is the lowest level at which it appears.

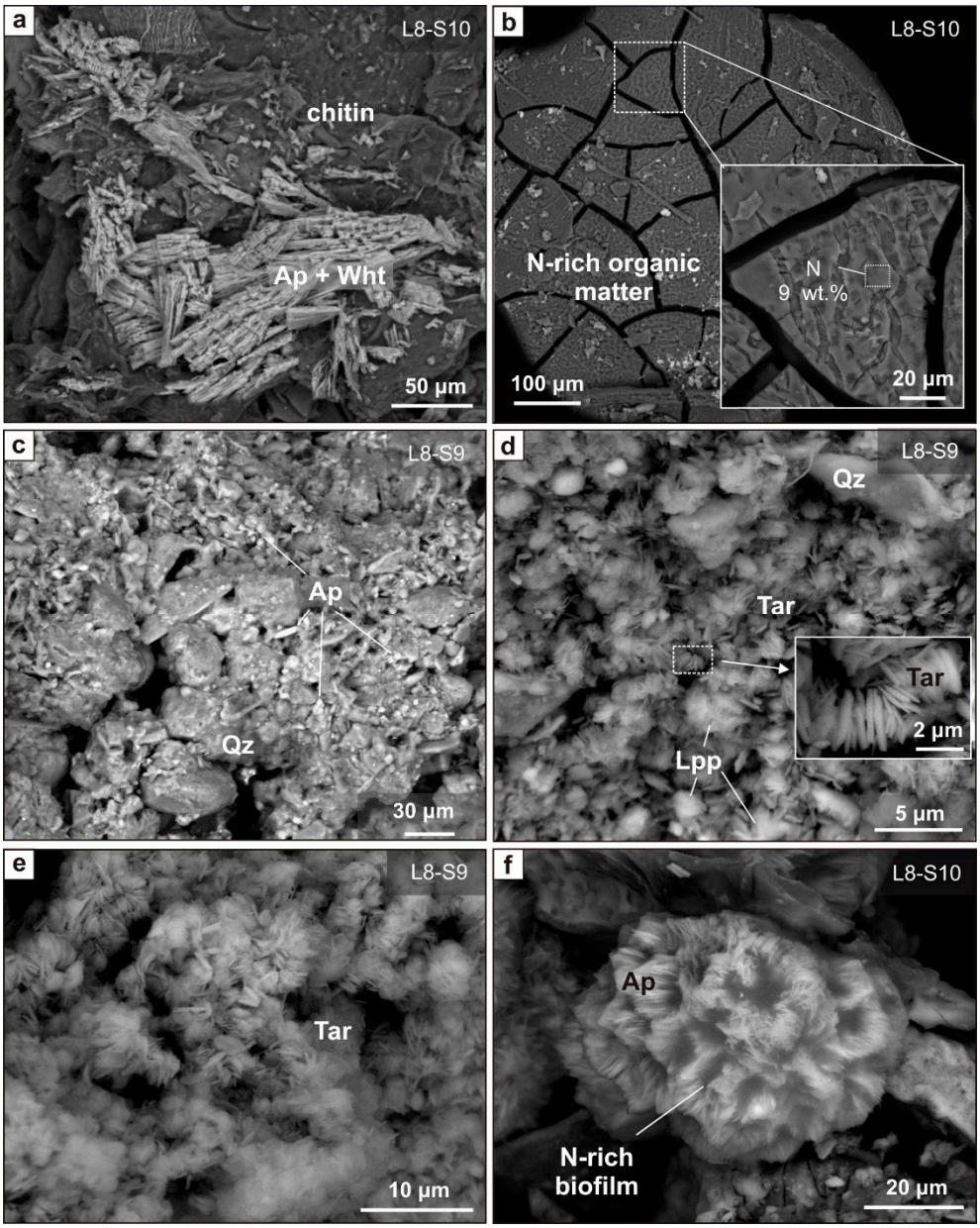

Figure 14. Back-scattered electron (BSE) images showing the diversity of phosphates and organic matter remnants from layer 8, East Chamber of Denisova Cave. (**a**) Intergrown fan-shaped apatite and whitlockite on the surfaces of chitin particles. (**b**) Slice of N-rich organic matter. (**c**) Fine-grained apatite cementing sandy particles. (**d**) Euhedral platy taranakite and tiny leucophosphite clots cementing siliciclastic matter. (**e**) Lace-like aggregate of platy taranakite. (**f**) Tiny spherulites

consisting of needle-like apatite (dahllite ?). Ap = apatite, Lpp = leucophosphite, Qz = quartz, Tar = taranakite.

The base of layer 8 is composed of brown matter rich in siliciclastics with predominant sandy particles (Figures 7 and 14c,d) and <20% phosphates in total, mainly fine apatite that cements sand grains. Taranakite appears as euhedral platy crystals cementing ≤2 mm almost monomineral aggregates of sand grains (Figure 14d,e). Fine anhedral particles of leucophosphite are also present.

Apatite is morphologically unusual and occurs uniquely in this layer as clots of aggregated 10–40 μm spherulites composed of needle-like grains (Figure 14f). The spherulites consist of apatite, sand grains, and/or fragments of chitin coated with N-rich (3–7 wt%) biofilms (Figure 15).

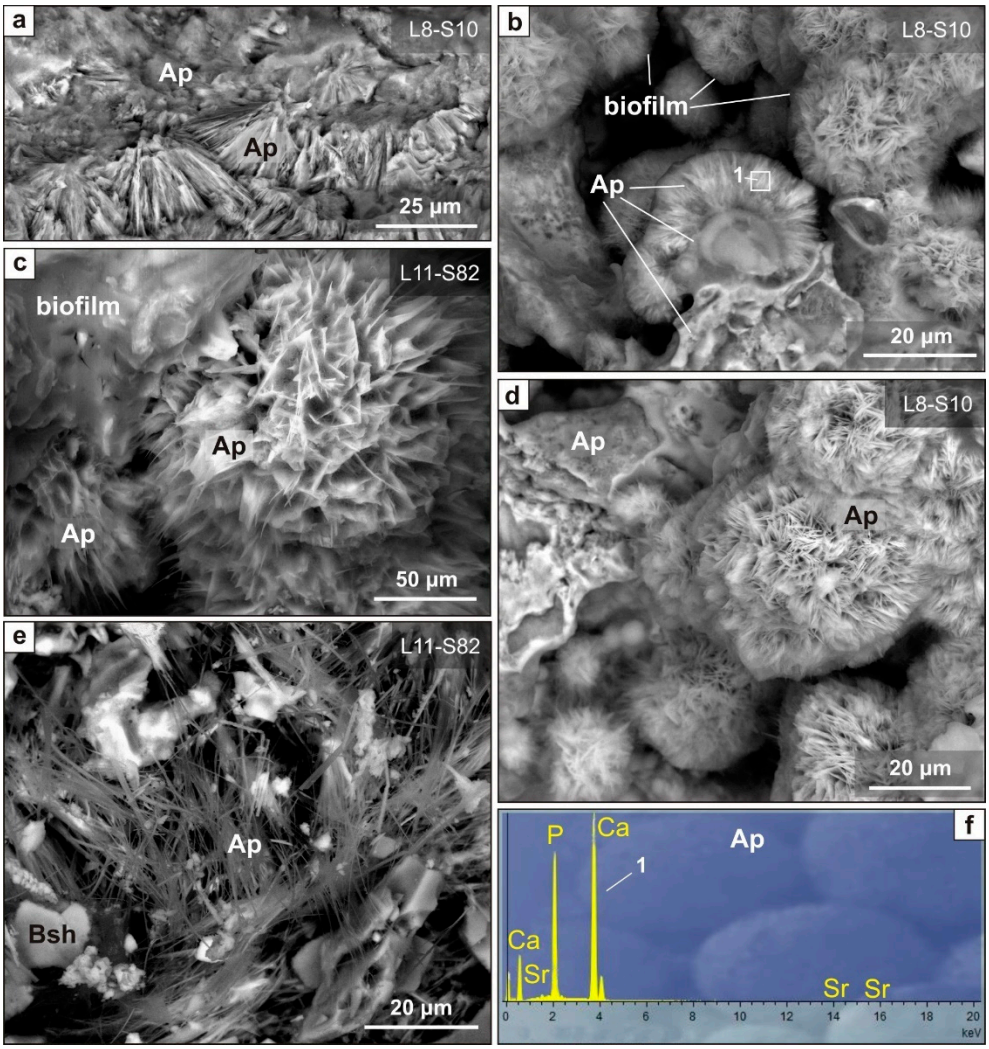

Figure 15. Back-scattered electron (BSE) images showing the morphology and typical EDS spectrum of apatite, East Chamber of Denisova Cave. (**a**) Massive apatite alternated with aggregates of apatite spherulites. (**b**–**d**) Aggregated spherulites of needle-like apatite (dahllite ?), with massive apatite in the cores (**b**) and with biofilms over the spherulite surfaces (**b**,**c**). (**e**) Acicular apatite occupying interstices between brushite crystals. (**f**) Typical EDS spectrum of apatite (in keV). Ap = apatite, Bsh = brushite.

High-quality analyses of apatite were impossible because of very small grain sizes and complex morphology of aggregate surfaces, although quite a stable Ca/P molar ratio of $X_{av.}$ = 1.77 (1.64–1.87; n = 18) was obtained (Figure 15f), fitting into the range common to

dahllite (X = 1.55–1.85) [75]. The spherulites are morphologically identical to hydroxylapatite grown from pH ≈ 6 solutions of Ca and Mg nitrates and $(NH_4)_2HPO_4$ [76].

Layer 9, ~30–40 cm: soft pale yellow to light brown material with siliciclastic particles more abundant than in other layers and moderate amounts of phosphate nodules. Sediments change in particle size, assemblage of authigenic phosphates, and percentage of siliciclastic matter from the top to the base of the layer (Figures 4, 6 and 7). In the upper part (samples 8 and 7), <1 mm phosphate nodules coexist with abundant and coarser 2–5 mm aggregates of taranakite (22–25%), leucophosphite (4–5%), and monetite (2%) (Figures 7 and 16a–e).

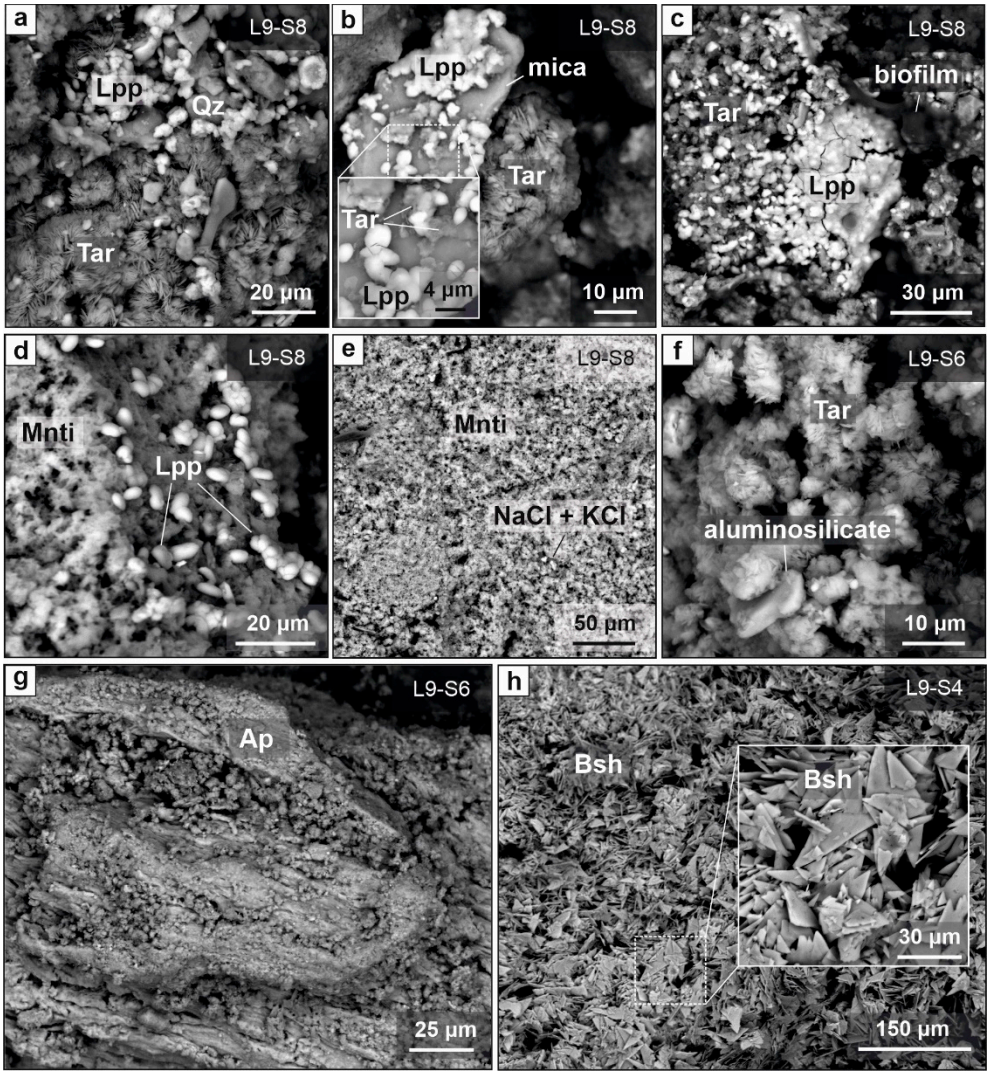

Figure 16. Back-scattered electron (BSE) images showing the diversity of phosphates from layer 9, East Chamber of Denisova Cave. (**a**–**c**) Aggregates of platy to tabular taranakite and rice-like leucophosphite clots. The surfaces of K-Al-Fe^{3+} phosphate aggregates are often coated with biofilms. (**d**,**e**) Porous aggregates of fine monetite. (**f**) Lace-like aggregate of euhedral platy taranakite. (**g**) Nodule of anhedral apatite. (**h**) Aggregate of randomly oriented platy brushite with sharp edges and flat faces. Ap = apatite, Bsh = brushite, Lpp = leucophosphite, Mnti = monetite, Qz = quartz, Tar = taranakite.

Samples from the middle of the layer (sample 6) contain phosphate nodules of more uniform sizes (<1 mm), with up to 45% taranakite, 4% monetite, 10 % apatite, and microscopic clusters of leucophosphite particles (Figure 16f,g). The percentage of siliciclastics in this part of the layer is the lowest: 40% vs. 64–71% in the other part of the layer. Sample 4 from the layer base contains 5–10 mm phosphate nodules (Figure 4) of a different composition, with apatite as a main phosphate phase (20%), taranakite reduced to 4%, and

brushite (12%) appearing for the first time in the section (Figures 16h and 17a). No monetite or leucophosphite was observed at this level.

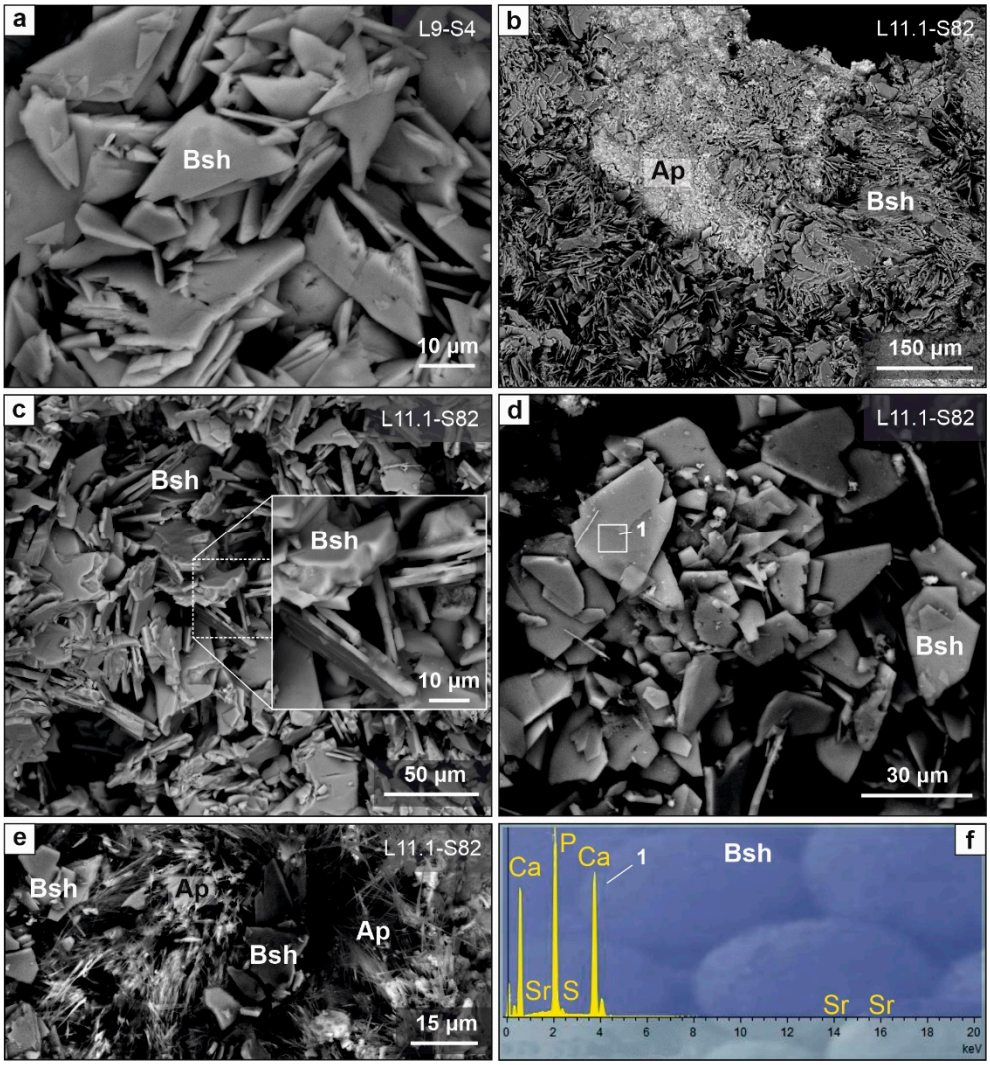

Figure 17. Back-scattered electron (BSE) images showing the morphology and typical EDS spectra of brushite, East Chamber of Denisova Cave. (**a**) Aggregate of randomly oriented typical platy triangular brushite. (**b**) Platy to tabular brushite encrusting massive apatite. (**c,d**) Lace-like intergrowths of typical tabular brushite. (**e**) Petal-shaped aggregates of brushite with interstitial acicular apatite. (**f**) Typical EDS spectrum of brushite (in keV). Ap = hydroxylapatite, Bsh = brushite.

Taranakite appears at least twice in phosphate nodules from the upper part of layer 9, i.e., before and after leucophosphite (Figure 10). Predominant early taranakite occurs as typical rose-like aggregates of ≤7 μm euhedral platy crystals. Lace-like taranakite cements sand grains, where sporadic mica plates are occasionally preserved (Figure 16a,b). Leucophosphite (≤10 μm rice-like grains) occupies the interstitial space between rose-like taranakite aggregates or grows over siliciclastic fragments (Figure 16a–d). Locally, leucophosphite coalesces in a ≤2 μm crust with fine platelets of later taranakite precipitated on its surface (Figure 10d,f). The intergrowths of K-Al-Fe^{3+} phosphates are coated by biofilms with 3.4–3.8 wt% N. Like almost all natural samples, taranakite from Denisova Cave shows very limited substitution of Ca and Sr for K, as well as Fe^{3+} for Al [46]. It contains impurities of SrO (up to 1.6 wt%), CaO (up to 3.4 wt%), and Fe_2O_3 (commonly ≈ 1.5 wt%; up to 5.7 wt%), as revealed by SEM-EDS (Table 4 and Figure 10e).

Micrometer apatite and monetite occur as pumice-like aggregates with rice-shaped anhedral μm-size grains of leucophosphite on their surfaces (Figure 16d,e). Brushite was

found at the base of layer 9 as lace-like but solid monomineral aggregates of randomly oriented ≤60 μm triangular platy crystals with acute edges and flat faces (Figures 16h and 17a).

Layers 11.1 and *11.2* (top, samples 3, 2, 1; 82): Ca phosphates (brushite and apatite) mainly replace limestone fragments, forming thick reaction rims (Figure 18).

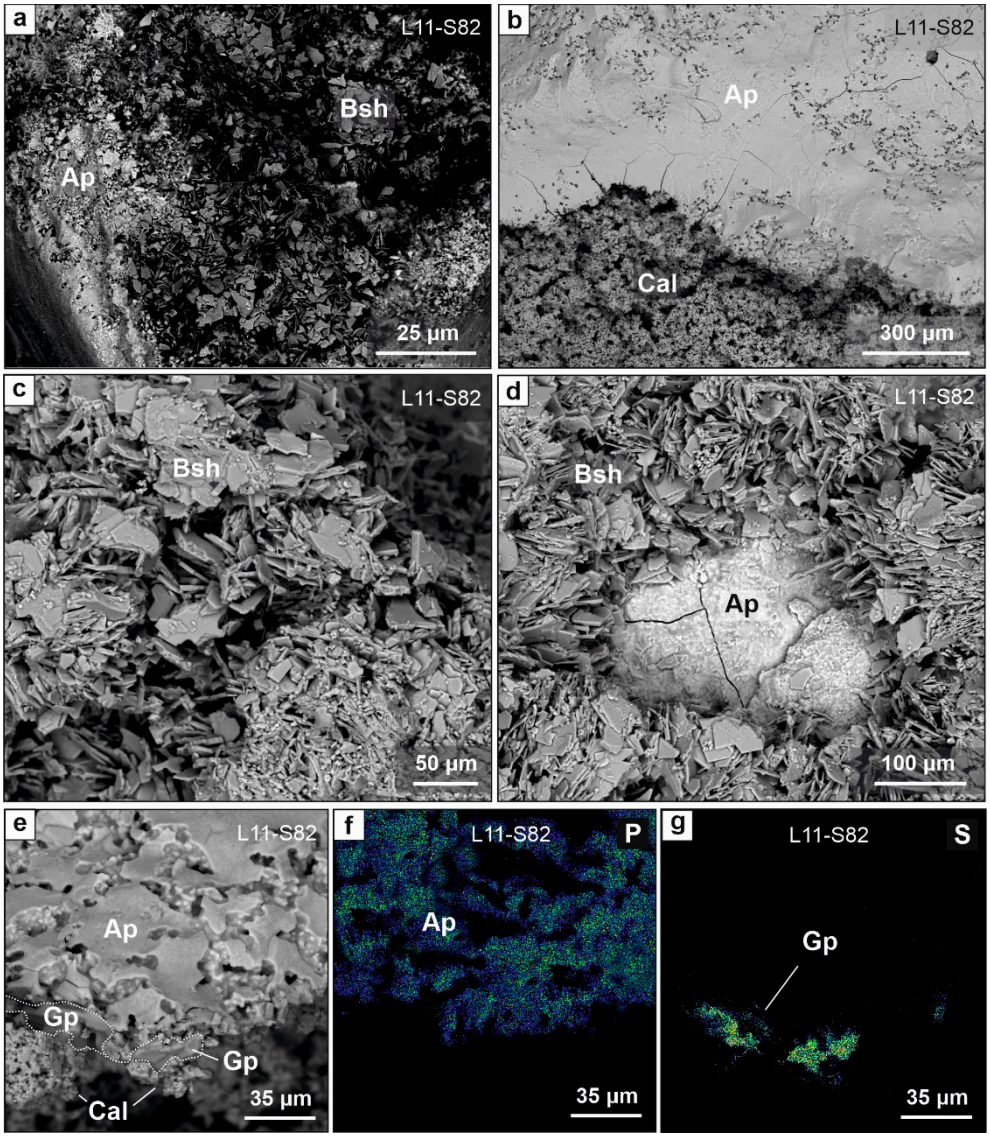

Figure 18. Back-scattered electron (BSE) images (**a**–**e**) and element maps (P, S) (**f**,**g**) showing the diversity of phosphates from layer 11, East Chamber of Denisova Cave. (**a**) Aggregate of platy brushite encrusting massive apatite. (**b**) Reaction rim of porcelain-like apatite on a porous limestone. (**c**) Lace-like aggregate of randomly oriented platy brushite. (**d**) Contact of typical platy brushite and a dense apatite. (**e**–**g**) Contact of etched limestone and phosphatic zone. Newly formed apatite and gypsum inherit the cavernous texture of etched calcite. Ap = apatite, Bsh = brushite, Cal = calcite, Gp = gypsum.

Coarse fragments in layer 11.1 are almost fully replaced (Figures 2 and 3). The surviving relicts of limestone are heavily leached to convert into vuggy aggregates (Figure 18b). The bulk samples of soft sediments contain no more than 1% of calcite. Brushite occurs as lace-like aggregates of randomly oriented ≤40 μm platy crystals, mostly with {010} faces and sharp edges, varying in color from white–ivory to yellow–ivory (Figures 17b–e and 18a,c,d), often formed in different episodes of nucleation and growth. Apatite appears as extremely thin filaments among predominant brushite (Figures 15e and 17e), which is

chemically pure, with impurities limited to SrO (0.6–1.5 wt%) and SO_3 (up to 1.5 wt%) (Table 4). Brushite aggregates occur as loose, thick replacement zones, often with dense massive apatite at the contact and with a composition close to that of $Ca(HPO_4)\cdot 2H_2O$ (Figure 17f).

Apatite is the only phosphate in layer 11.2 forming stable assemblages with calcite that increases with depth (Figure 7). According to SEM-EDS analyses of massive apatite from reaction rims after limestone, P_2O_5 approaches its content in stoichiometric hydroxylapatite (42.4 wt%), whereas CaO is much below the stoichiometry (47.3 vs. 55.8 wt%). The Ca/P molar ratio is likewise lower than that in stoichiometric hydroxylapatite (1.33 to 1.50 ($X_{av.}$ = 1.40; n = 15) vs. 1.67), which makes Ca phosphate from layer 11.2 in the East Chamber similar to Ca-deficient hydroxylapatite ($Ca_{10-x}(PO_4)_{6-x}(HPO_4)_x(OH)_{2-x}$). This hydroxylapatite variety can easily incorporate as both F^-, Cl^-, $(CO_3)^{2-}$, $(SO_4)^{2-}$ anions and Na^+, Mg^{2+}, K^+, Sr^{2+}, Zn^{2+} cations [77,78]. Apatite from the replacement crusts contains Sr ($X_{av.}$ = 1.0 wt%; up to 1.3 wt% SrO) and SO_3 (X_{av} = 1.2 wt%; up to 2.2 wt%) at most of analyzed points, as well as, locally, Zn (up to 0.6 wt% ZnO) and Cl (up to 0.3 wt%). The impurities of Al, Si, Na, and Fe are most likely associated with siliciclastic contamination, whereas the coincidence of K and Cl spikes may be due to the presence of tiny sylvite inclusions. Apatite from layer 11 exhibits the broadest reflections, with a main diffraction peak at 2 theta of 31.7–32.0° (Cu$K\alpha$) and has the lowest intensity compared to the XRD patterns of all other apatite-containing samples. The lower peak intensity in this case is due to the poor crystallinity of ultrafine Ca-phosphate [79,80]. The XRD pattern of this apatite is very similar to that of Ca-deficient hydroxylapatite of low crystallinity (00-046-0905, database PDF-2 [81]).

6.4. Effect of Phosphate Leaching on Stone Tools

A stone tool manufactured from a dark gray homogeneous massive microcrystalline (5–50 μm) hornfels was found in layer 9 of the East Chamber sequence (Figures 19 and 20).

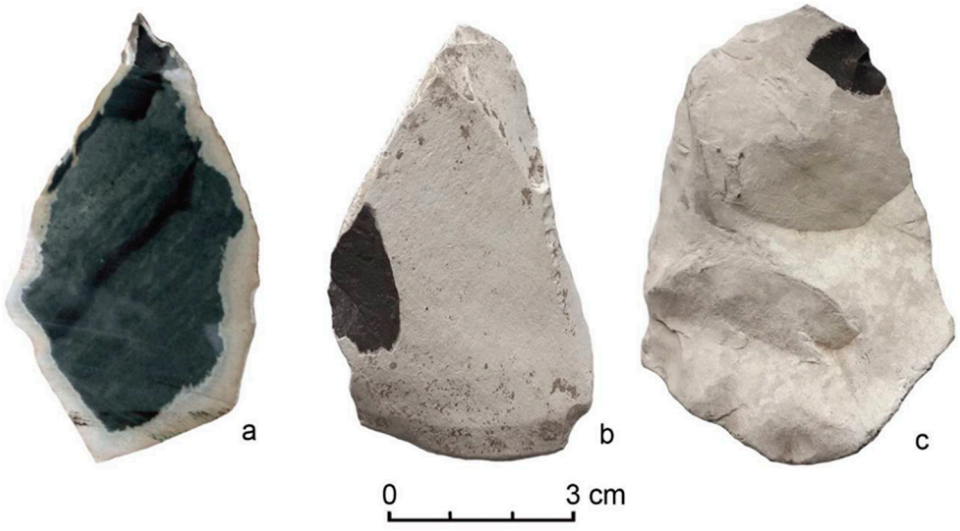

Figure 19. Partially replaced paleolithic stone tool manufactured from a hornfels with a white mainly crandallite coating (layer 9, East Chamber). (**a**) Core, (**b**,**c**) Flakes.

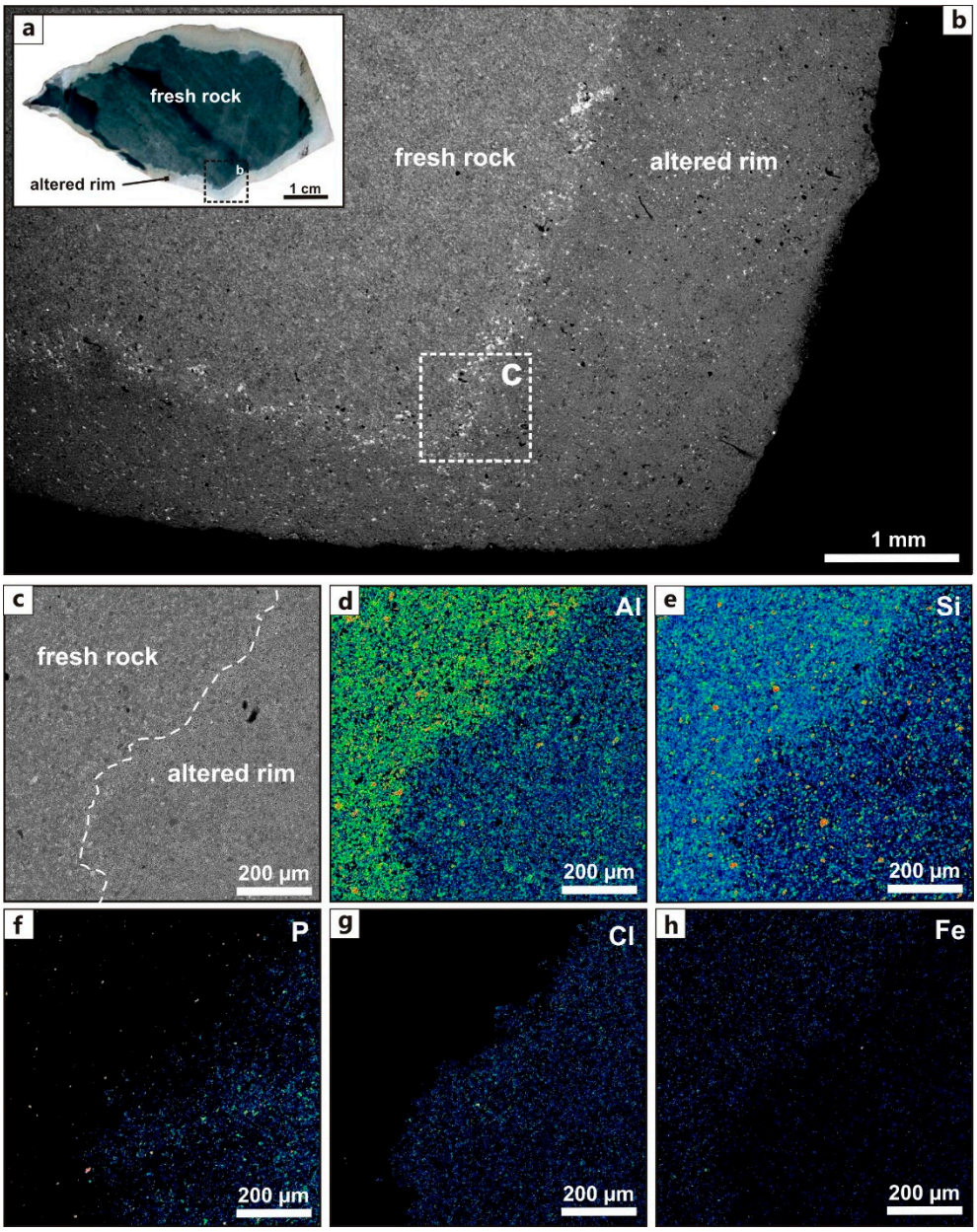

Figure 20. Paleolithic stone tool manufactured from a homogeneous hornfels with phosphatized alteration rim (layer 9, East Chamber). (**a**) Cut surface of stone tool: massive fresh dark gray interior and a white coating of altered material (mainly crandallite ± dahllite, gypsum, and calcite). (**b**–**h**) BSE image (**b**,**c**) and Al, Si, P, Cl, and Fe elemental maps (**d**–**h**) of stone tool with a crandallite ± dahllite, gypsum, and calcite rim.

The rock consists of quite uniformly distributed pyroxene, amphibole, plagioclase, potassium feldspar, and quartz, with trace amounts of apatite, gypsum, and calcite identified by XRD in a white rim coating of fine secondary crandallite $CaAl_3(PO_4)(PO_3OH)(OH)_6$. The crandallite aggregate is commonly dense, with some of thick (≤1 cm) reaction rims with a microporous periphery. Relicts of primary silicates rarely preserve at the back of the alteration front. The outer and inner boundaries of thin (≤5 mm) rims are roughly parallel and generally mimic the tool contours, whereas those of 5–10 mm thick rims are non-parallel, and the boundary between fresh and altered material is uneven (Figure 20). The interior of the tool is fresh, which was confirmed by SEM-EDS examination.

7. Discussion

7.1. Authigenic Phosphates in Sedimentary Sequence of East Chamber: Diversity and Formation Conditions

Cave sediments can inherit phosphorus from two main organic parent materials: (i) guano (mainly of insectivorous bats) as a source of organic acids, P, N, and S and (ii) bone apatite as a source of Ca and P [11]. Bat guano was proven to be the most important parent material of P enrichment in a great number of minutely investigated caves worldwide [1,45], although protein from dead animals may be a minor source of P.

The sampled Late Pleistocene–Holocene sedimentary sequence in the East Chamber of Denisova Cave includes at least three ≤2 cm layers of degraded bat guano at the top of layers 6 (sample 15), 7 (sample 13a), and 8 (sample 10). They are all of deep black color due to degraded N-rich organic matter ($C_{org.}$—3.4–27.8 wt%; N—0.5–7.9 wt%) (Table 3) and contain fragments of insect chitin (Figure 5).

Because meter-thick primary guano layers commonly reduce to 1–2 cm after complete degradation [1], the black layers in the East Chamber section may remain from an at least 2 m thick original layer of bat guano deposited at a rate of 2 to 10 cm/yr. In the case of Denisova Cave, it is reasonable to assume minimal (2 cm/yr) deposition rates, given the climate conditions of the region and the sizes of bat colonies (n·1000 individuals) that winter in caves in southern Siberia [38,39]. Correspondingly, the organic- and P-rich parent matter for each of the black layers in the East Chamber accumulated for no less than 100 years. Thus, large colonies of insectivorous bats inhabited Denisova Cave in at least three episodes from the Early (≈10 kyr BP) to Middle (≈5 kyr BP) Holocene (Figure 21). In addition to the preserved insect exoskeleton (chitin) fragments in the thin black layers, the phosphate-silicate cave sediments bear Ca phosphate pseudomorphs after chitin particles, which are abundant in layer 7 but are few in the top of layer 9. Therefore, smaller groups of insectivorous bats apparently lived in Denisova Cave during the deposition.

This inference has an archaeological implication that people did not interfere with the life of bats, i.e., they either abandoned the cave or their presence was limited to short visits. Thus, our data prove the hypothesis that for some reasons, people did not occupy Denisova Cave on a regular or long-term basis in the early Holocene, although humans lived over much of the Altai territory at that time. The Early Holocene human occupation of the area is known from a wealth of archaeological evidence, including from caves in the vicinity of Denisova. Such evidence includes archaeological remains from layer 10a in Kaminnaya cave (15 km from the Denisova site) corresponding to Pleistocene/Holocene transition, with several available radiocarbon dates of 8850 ± 120 yr BP (SOAN—3700) and 8685 ± 100 yr BP (SOAN—3701) [82], as well as Neolithic artefacts (including a burial) in the layers above. An early Holocene age was also inferred for stone tools from layer 4a in Iskra cave 25 km far from Denisova [83], as well as for those from Biyke cave in central Altai, 100 km from Denisova [83]. In general, early Holocene archaeological evidence in the Altai has been mostly obtained from open-air sites (Karaturuk, Ust-Sema, Ust-Kuyum, Maima, Ust-Biyke, etc.). The following Neolithic period marked by the appearance of the first ceramics has been documented largely in tens of living and burial sites in the mountainous, piedmont, and forest steppe areas of the Altai. The reasons that made early Altai people leave Denisova Cave remain yet unclear.

The complete cycle of guano biodegradation in the arid climate of Israel (Etzba Cave) takes only ten years [1]. In warm climates, fresh guano and urea rapidly decay through bacterial and fungal decomposition, releasing large amounts of water, CO_2, H_2S (and other sulfuric gases), and NH_3 [3,44]. Commonly, organic matter decomposes rapidly, and its content is largely lost within a few cm depth to >40 wt%, and N and S in degraded matter decrease considerably as well. Strongly acidic environments are typical of guano sequences, as bacterial respiration releases organic acids (mainly acetic and formic acids) and alcohols, whereas sulfur oxidizing bacteria produce sulfuric acid [1,45].

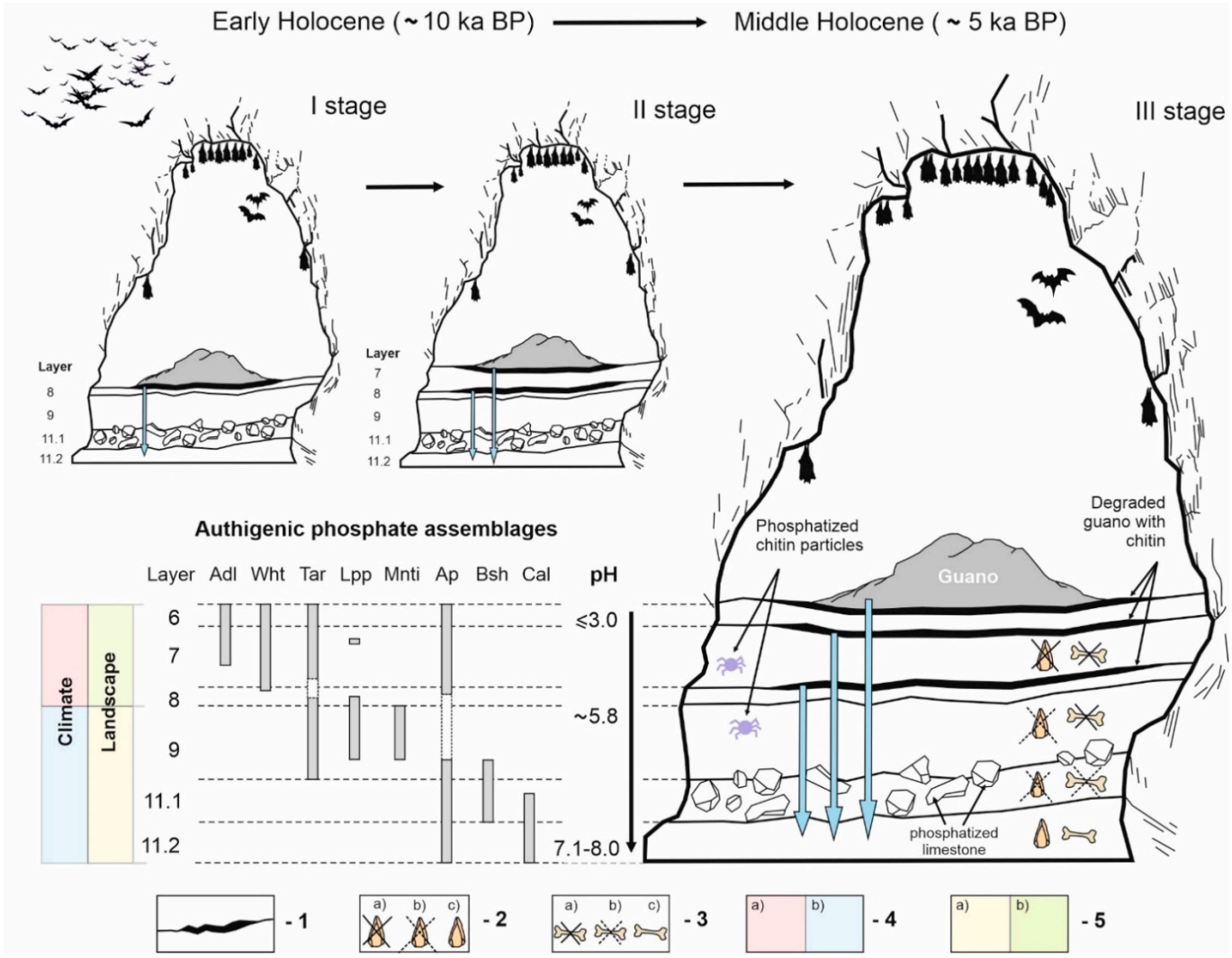

Figure 21. Formation model of Holocene authigenic phosphate mineralization in sediments in the East Chamber of Denisova Cave (Altai). Climatic and landscape reconstructions. Dates are according to [9,30]. 1 = black layers of degraded N-rich organic matter with abundant authigenic phosphate mineralization and well-preserved chitin particles in clay–sand–phosphatic sequence; 2 = no stone tools were found (**a**), partially replaced stone tools (**b**), and fresh stone tools (**c**); 3 = totally replaced (**a**), partially replaced (**b**), and intact (**c**) mammal bones; 4 = relatively warm (**a**) and relatively cold (**b**) climatic conditions; 5 = predominant steppe (**a**) and taiga (**b**) plant communities. Adl = ardealite, Ap = apatite, Bsh = brushite, Cal = calcite, Lpp = leucophosphite, Mnti = monetite, Tar = taranakite, Wht = whitlockite.

As a result of bacterial activity, solutions equilibrated with cave sediments become more acidic, to ≈3–4 pH [1]. The progress of bacterial activity and downward penetration of aggressive organic acids induces the decomposition of proteins and the dissolution of bone material in the guano layer and the sediments below. Eventually, phosphorus passes to the solution as $(PO_4)^{3-}$ and $(HPO_4)^{2-}$, and acidic phosphate solutions percolate down through the cave sediments. The percolation depth has several controls: (i) volume of bat guano, depending on colony size and occupation time; (ii) humidity, depending on local climate and cave type (for instance, no authigenic phosphates were found in dry Qumran Cave 24 in Israel [20] from an arid area adjacent to the Dead Sea); and (iii) lithology and porosity of the drained sedimentary sequence. As to the latter factor, acidic phosphate solutions can percolate to depths of a few meters through porous siliciclastic sediments because the neutralization reaction upon interaction with poorly soluble silicates is very slow [84,85]. Carbonate material (limestone or dolomite fragments from the cave walls

and ceiling) acts as a highly effective neutralizing agent that produces a pH profile from 2.7–4.1 at the top to 7.1–8.0 at the bottom of sediments beneath the guano layer, which correlates with the sequence of authigenic phosphates (Figure 21).

As the biodegradation of guano in the cave abandoned by insectivorous bats progressed, the cave sediments tended to reach steady state, which can be inferred from predominance of some mineral species or a stable authigenic phosphate assemblage [1,2]. The predominant phosphate phase depends mainly on residual acidity of the medium and available mineral-forming cations, which include Al (or K and Al) in siliciclastic, Fe-Al-(K) in iron-aluminous, and Ca in carbonate (or Ca-Mg in dolomitic karst) substrates; a mixed assemblage of phosphates may form in a mixed substrate. Diffusion profiles are commonly mosaic, with several mineral assemblages in local volumes within a single black layer. The history of a typical profile of phosphate leaching is described below and compared with that of the East Chamber of Denisova Cave.

Most of diagenetic transformations in sediments take place on the ground surface or soon after burial. Each mineral and mineral assemblage forms under specific conditions; therefore, their presence is indicative of the environment that prevailed at the time of formation [20]. Active microbial guano degradation leads to the formation of authigenic phosphates in situ in the upper cave sediments, which are stable under acidic and slightly acidic conditions. These phosphates include ardealite [57,71] and variscite [86], with solubility in the ranges of pH ≤ 3–5.5 and 3 < pH < 6, respectively, as well as taranakite. Taranakite can be synthesized from concentrated aqueous solutions at pH = 2.3–2.9 and forms during reactions of phosphate solutions with soil material at pH = 4–5 [84,87]. The phosphate assemblages can coexist with gypsum and nitranite in dry caves, but sulfates and especially nitrates dissolve and cannot survive in wet caves [1,57]. According to evidence from dry caves in Israel [1], Ca phosphates are uncommon in the upper 5 cm of the guano section but appear sporadically as reaction rims on limestone and dolomite fragments that buffer the acid phosphate leachates and can locally maintain higher pH values. Phases that form in these conditions are low-crystallinity analogs of carbonate-rich hydroxylapatite (dahllite). However, the investigation of guano-related minerals in twenty-two European caves with higher humidity suggested different inferences. The typical initial assemblage in fresh decaying guano is composed of brushite, ardealite, and gypsum [24].

Relatively few prehistoric caves have been well-documented in terms of authigenic assemblages: et-Tabun Cave [58] and Kebara Cave [20] in Israel, Theopetra Cave in Greece [88], and Cioclovina Cave in Romania [20,22,50,54,57,60,62,63]. The Denisova Late Pleistocene–Holocene phosphate record (eight phosphates and two sulfates) sheds light on many details of older diagenetic mineral-forming processes that developed in a flowing system under high vertical gradients of pH and P, Ca, and S concentrations.

Phosphates that would be stable in acidic environments (e.g., ardealite) occur more rarely in limestone-hosted prehistoric caves relative to Ca phosphates (Table 1) [1,57]. Bicarbonate waters equilibrated with carbonate host rocks of the caves drain the sediments for ages and millennia and move the water–rock equilibria toward a higher alkalinity of pH=7.0–8.5 [89], which induces dissolution of ardealite, variscite, and crandallite. However, abundant euhedral crystals of ardealite are present in layer 6 and at the top of layer 7 of the East Chamber (Figures 7, 8, 11, and 21). Flat hopper crystals of ardealite, which grow over earlier aggregates of fine whitlockite and low-crystalline apatite (Figures 9f, 11b and 13d), provide a good illustration of the general decreasing pH trend early during the bacterial degradation of bat guano from pH=5.1–7.3 in fresh guano to strongly acidic pH of 2.7–4.1 [3]. These unique findings indicate that the degradation process in the East Chamber has not been completed yet. Black biogenic layers at the top of layers 6 and 7 became rapidly buried under the following low-permeable siliciclastic layers. The absence of water infiltration preserved the rare ephemeral mineral of ardealite in the Middle Holocene cave sediments, as well as trace amounts of gypsum or even water-soluble polyhalite ($K_2Ca_2Mg(SO_4)_4 \cdot 2H_2O$) locally in the top of layer 7. Originally, ardealite could also

exist in the black layers at the top of layers 8 and 9, but it was dissolved as guano was totally decomposed and the solutions became less acidic. Its crystals show obvious signatures of dissolution at the top of layer 7 (Figure 9b,c).

The layers with ardealite have a number of other fingerprints: high contents of sulfur (1.14–4.78 wt% SO_3), N-rich organic matter, and chitin fragments (Tables 2 and 3, Figures 5 and 6). The primary guano layers likewise inherited notable enrichment with essential elements, such as ZnO (up to 0.57 wt%) and CuO (0.04–0.07 wt%), relative to the underlying cave sediments (0.03–0.05 wt% ZnO and <0.02 wt% CuO at the top of layer 11) (Table 2). The black layers have Zn concentrations comparable with those from Borneo caves (≈2000–6000 ppm Zn) [3].

The acid potential of solutions leached from biodegraded bat guano was considerably neutralized at the level of layers 8 and 9. In addition to pH of pore solutions, the phosphate assemblages at specific layers were controlled by major-element chemistry of sediments. Ca-rich sediments from the top of layer 8 are dominated by whitlockite and hydroxylapatite of low crystallinity. Layer 8 was the only layer in which tiny spherulites of hydroxylapatite coated with N-rich biofilms was discovered (Figures 14f and 15b-d). The spike in apatite generation was apparently due to high microbial activity in degrading guano, as apatite from this layer is morphologically identical to that produced in organic-rich medium [90]. The predominance of whitlockite over apatite at this level likewise may result from high organic (protein) and Zn enrichment of its growth medium. Zn-substituted whitlockite is able to crystallize from media with unusually high Ca-to-Zn ratios, from 9 to 30 [91]. Whitlockite from Denisova Cave also bears an unusual Cu impurity. Note that Zn and Cu, which obviously came from proteins (enzymes), inhibit the growth of apatite but do not impede crystallization of whitlockite [91].

Further down in the section (to the base of layer 9), taranakite becomes the predominant K-Al phosphate (Figure 7). This is a lithologically exceptional sedimentation rhythm, as it is in layer 9 that the amount of siliciclastic (mainly sandy) matter and the related SiO_2, Al_2O_3, TiO_2, and Fe_2O_3 contents increase and K_2O reaches its maximum (up to 5.6 wt%), whereas CaO and MgO decrease to the lowest values of 3.9 wt% and 0.05 wt%, respectively (see paragraph 6.1). High sand percentages in this interval may be due to airborne dust during in the climate of the last glacial maximum (LGM, MIS 2) [9].

In phosphate-rich acidic environments, taranakite becomes stable relative to clay minerals. As the least soluble among the considered phosphates, it is among the ultimate end products of phosphate immobilization in soils and fine-grained siliciclastic sediments. This mineral is mainly precipitated and occurred in a poorly drained argillaceous matrix [84]. Its percentage in the East Chamber deposits reaches 45 wt% at the −209 cm level, where mica falls down to 7 wt%. Leucophosphite, a very rare mineral species, is the second K-bearing hydrous phosphate in the studied cave sediments. Although unstable relative to Al hydroxyphosphates [84], leucophosphite is common to the layers with the highest iron content (3.6–5.2 wt% Fe_2O_3). In the East Chamber sediments, it formed after taranakite; very rarely, trace amounts of taranakite are precipitated on the surfaces of leucophosphite globules (Figure 10d). The formation conditions of phosphates in carbonate and shale sediments are well illustrated by the phase diagram of the Ca-P-Al-K-O system [20]. Namely, taranakite is stable at low to moderate concentrations of $(HPO_4)^{2-}$ (10^{-5}–10^{-2}) under slightly acidic to nearly neutral pH, whereas hydroxylapatite is a stable phase in neutral to subalkaline environments; as $(HPO_4)^{2-}$ increases to above 10^{-2}, taranakite becomes stable at pH > 7. The absence of apatite in assemblages with K-Al-Fe^{3+} hydrophosphates indicates pH of about 6 in pore waters [84]. Al^{3+} and Fe^{3+} show limited isomorphic substitutions in taranakite and leucophosphite, as was reported for natural minerals [46] and confirmed for their synthetic counterparts [92].

Crandallite, a hydrous Al and Ca phosphate, was never found in the sampled section as a member of authigenic phosphate assemblages. According to the Ca-P-Al-K-O diagram [20], the size of the crandallite field is mainly controlled by Al activity. This phase probably grows from nearly neutral to slightly acidic solutions (pH = 6–7) with quite low

activity of $(HPO_4)^{2-} < 10^{-3}$ and relatively high activity of $Al(OH)_4^-$ (10^{-6}–10^{-8}). This composition of pore waters is very unusual for soil profiles, and it appears quite reasonable that crandallite was found in reaction rims after aluminosilicate rocks only once—in the hornfels tool (Figure 20).

Apatite is a dominant or single phosphorus phase at the bottom of the phosphate profile in karst cave sediments, where soluble P-bearing compounds can be delivered and where the total alkalinity in the water–rock system is buffered by Ca carbonate at the pH level of 7.1–8.0 (Figure 21). The zones of predominant phosphates in sedimentary sequences from karst caves (i.e., in systems with bulk Ca excess) mark the paleo level of the deepest drainage with soluble waste products derived from biodegraded bat guano. The formation of mono- or bimineral zones composed uniquely of Ca phosphates means that biodegradation has been completed [1]. Authigenic (CO_3)-bearing hydroxylapatite predominant in such profiles is stable only at pH ≥ 8 [79]. As reported by Shahack-Gross et al. [1], such apatite (dahllite) dominates over other phosphates 10 cm below the surface in seasonally occupied karst cave Ornit (Israel). It is the only phosphate over the whole profile (*H* = 3–29 cm) of Etzba karst cave (Israel), which insectivorous bats left ten years before sampling. The restricted depths of phosphate leaching in these caves are due to a very dry climate in the area. In Denisova Cave, the total thickness of the leaching profile reaches ~150 cm. The zone of predominant Ca phosphates starts at the base of layer 9 (h = −216 cm; Ap + Bsh) and spans layer 11.1 (h = −227 cm; Ap + Bsh) and the top of layer 11.2 (h=-236 ÷ −246 cm; Ap). Numerous limestone fragments in these layers are almost totally replaced by Ca phosphates (Figures 2 and 3).

Thus, the boundary between layers 9 and 11.1 in the East Chamber sequence is at the same time a stratigraphic and lithological interface, as well as a geochemical barrier. The precipitation of Ca phosphates at that boundary started with bulk crystallization of metastable brushite (Figure 7). The solubility of $Ca(HPO_4)\cdot 2H_2O$ at pH = 8 (T = 37 °C) is about five orders of magnitude higher than that of apatite; however, unlike apatite, it can crystallize since pH = 6 [93]. Due to kinetic factors that control nucleation and growth rates, brushite can precipitate in media rich in P, especially in the presence of Mg^{2+}, which inhibits the growth of hydroxylapatite [94]. Brushite crystals were synthesized from several kinds of solutions: nitrate and ammonia solutions [93], which can be considered as model analogs of solutions early during guano biodegradation; analogs of biological media; and aqueous solutions enriched in inorganic compounds, namely Sr [95]. The brushite crystals have diverse morphology depending on the growth media composition. In the Denisova deposits, it occurs as monomineral lace-like aggregates of thin platy crystals (Figures 17 and 18). Their particular morphology is identical to that of brushite synthesized from solutions enriched in organic compounds [95].

7.2. Preservation of Archaelogical and Paleontological Findings in the East Chamber: Biogenic Processes and Acidic Leaching

Excavations in the East Chamber of Denisova Cave (2004–2016) yielded more than 80,000 stone tools made of various rock types and 200,000 whole or fragmented bones of large mammals. The findings were abundant in the lower cultural layers of the chamber but fewer in the middle and upper layers. The amount of excavated material per 1 m^2 was 3000 and 3300 stone artefacts and bone remains, respectively, in Early–Middle Paleolithic layers 15 and 14; 300 and 550 pieces in layer 13 to 900 and 2200 pieces in layer 11.3, respectively, in the Middle Paleolithic interval; and 350 and 1500 pieces, respectively, in the upper part of layer 11 (11.2 and 11.1).

The bone material is, in general, well-preserved in the lower and middle parts of the Pleistocene sequence. Bones are solid and vary in color, mainly from gray and light brown to reddish or, rarely, yellowish. The preservation state of bones may vary within a layer depending on the properties of the host sediments and specific taphocenoses. The bones digested by large carnivores, mainly cave hyenas and wolves, are the worst preserved and bear signatures of digestion and biting [9,96]. The perfect preservation of organic material

in Denisova Cave allowed DNA sequencing from bone remains from Pleistocene sediments older than 200 kyr BP [25,27,97–100].

However, the situation is quite different in the upper Pleistocene and lower Holocene intervals, with abundant authigenic phosphates. The findings are much fewer at the top of the Pleistocene interval (150 stone tools and 100 bone fragments per square meter in layer 9; P_2O_5 ≈ 11–32 wt%, mainly in the lower part, with ≈16 wt% P_2O_5) and lacking from Holocene layers 8–6 (11–33 wt% P_2O_5). Even hornfels tools in layer 9 are coated with thick reaction rims of crandallite (Figures 19 and 20) [101]. Meanwhile, the overlying Late Holocene deposits (layers 5–3) bear numerous well-preserved Bronze Age and Iron Age artefacts, as well as medieval objects of ceramics, stone and bone tools, metal items, and animal bones. Thus, the interval where archaeological and paleontological findings have been damaged and/or eliminated coincides with that of strong acidic leaching and coupled abundant phosphate mineralization (Figure 21).

Bones are commonly lacking in sediments highly enriched with phosphorus, except for few findings of powdered tubular bones that belonged to large mammals in the intervals of weaker phosphatization, although notably preserved worse than in older layers (11.3–17) free from phosphates. Thus, it is reasonable to hypothesize that the poor preservation or absence of bones (and hence DNA) [32,99] result from organic and phosphorus acids percolated down the sediments and their leaching.

Experiments by Berna et al. [19] showed that bone apatite is stable at pH > 8.1 but recrystallizes at pH 8.1 to 7.4 and often becomes replaced by more stable (e.g., F-substituted) species if the chemistry of the accommodating medium is favorable. As pH falls to below 7, apatite begins to dissolve, and the dissolution rates progressively accelerate upon further pH decrease [18]. Dissolved bone material becomes an important additional source of phosphorus for authigenic cave phosphate mineralization at pH ≤ 3 in media produced by degrading guano in the underlying sediments. At the same time, bone apatite remains stable at moderate alkalinity provided by the $CaCO_3$ buffer [19,21], which maintains good preservation of bone material in sediments rich in limestone or dolomite debris, even if P-rich leachates penetrate to that level.

According to our data, bone material in Middle Pleistocene sediments from the East Chamber remained preserved due to a natural geochemical barrier produced by collapsed limestone fragments embedded into layer 11 of cave deposits. The limestone debris occurring uniformly over the 30–40 cm thick layer neutralized all acidic solutions percolated from above, and phosphorus became immobilized. The completion of the guano degradation process is marked by the presence of a calcite + apatite assemblage [1].

The zonation of authigenic phosphate assemblages in the East Chamber deposits highlights the general trend that pH of P-rich leachates increases with depth from 3 to 8, which means that the upper part of the profile is immature. On the other hand, the relatively long postdepositional period (~5 kyr) makes us look for explanations of this trend. The profile formation and the contours of the phosphate-rich zone depend on the availability of main mineral-forming ions, as well as on local hydrology. The processes of precipitation, recrystallization, and subsequent dissolution/substitution of phosphates are especially rapid in zones of water leakage, where solutions are more abundant and contain higher concentrations of mineral-forming elements [24]. The preservation of partially degraded organic matter, the abundance of authigenic phosphates stable in acid media in layers 6–8, and sporadic findings of water-soluble salts provide reliable proofs for low humidity at these levels in Denisova Cave after the deposition. Furthermore, the layers of degraded bat guano soon became buried under dense clay sediments and thus isolated from atmospheric moisture.

Diagenetic mineral formation in karst caves is especially active within the ceiling area but becomes slower toward the walls of chambers and in the entrance area [1,24]. In caves inhabited by large bat colonies, guano dumps likewise form beneath the ceiling where most of the bats roost and wherefrom urine and waste products of guano degradation (including H_2O) leach downward. The distribution of phosphates in the sediments of the

East Chamber, in a way, mirrors the primary profile of the guano dumps. The discovery of at least three layers with abundant degraded OM, chitin particles, and authigenic phosphates stable in acidic environments indicates that the underlying section of cave deposits underwent active acidic leaching by P-rich solutions at least three times during the post-deposition history. The sediments of layer 6 were exposed to a single "acidic wave", whereas layer 9 underwent three episodes of alteration (Figure 21). The solutions of the first wave had the lowest pH and were apparently the most aggressive to organic remains. The following waves of phosphate leachates had been partly neutralized when reacting with the rocks on their way. Unfortunately, this postdepositional history leaves little chance to find well-preserved bone remains. Indeed, ZooMS analyses performed on bones from layer 9 resulted in a high rate of samples that could not be taxonomically identified, with more than 35% failing to produce enough collagen [98]. This high failure rate is likely due to heavy leaching of the sediments, which previously impeded OSL and ^{14}C dating, as well as genetic analyses of the materials from these layers [97].

7.3. Dissolved Bones: Source of Phosphorus in Cave Sediments

Bone material is another key source of phosphorus in cave deposits, besides guano. Dissolution of bone bioapatite (Figure 22) by highly acidic solutions released by guano biodegradation contributed a lot to the total Ca and P budget in sediments beneath the seepage front [1,20,21]. This inference can be illustrated by data on abundant bone material of bats that lived in Denisova Cave [102–105].

Figure 22. Fragments of a mammoth tusk diadem [105] found in the intermediate zone between phosphatized (**b**,**c**) and intact (**a**) sediments of layer 11, South Chamber. Degree of bone alteration depends on the intensity of phosphate leaching.

The death rate of young bats in cave colonies from areas of temperate and especially cold climates is as high as 30–50% [39,106], and the bodies remain in the places of occupation. This material is expected to be the most abundant in the area of guano dumps

beneath the ceiling. Indeed, the bones of *Chiroptera* predominate among bone remains of small mammals [103,104]. The Pleistocene taphocenosis of the cave contained eight species of bats, with dominant *Plecotus aff. Auritus* (56.3%), *Eptesicus* cf. *Nilssonii* (23.0%), and *Myotis dasycneme* (15.5%). The dead bodies are especially abundant in layer 22 of the Main Chamber, i.e., in the interval before the cave became occupied by humans, but their amount becomes about ten times smaller above layer 19 and remains at this level until the top of the Pleistocene section. Because the climate did not change much within that time span, the arrival of humans can be the only plausible explanation for the disturbance to the bat colony. The diversity of bat taxa reduces to four species in the Late Pleistocene (layers 19–9) and Early Holocene (layers 7 and 6) taphocenotic assemblages, although the Altai *Chiroptera* of that time counted nine species. Furthermore, the bone findings are two orders of magnitude fewer in layers 6 and 7: only eleven bat teeth vs. 2200 in Pleistocene deposits [9,102,103].

The Holocene intervals of degraded bat guano in the East Chamber, with abundant OM, chitin (and/or phosphate pseudomorphs after chitin), and authigenic phosphates, lack *Chiroptera* bones altogether. Preserved bones were found sporadically in fractures in limestone at the level of layers 6–9. The extremely high P and Ca enrichment of sediments in layers 6 and 7 (Figure 6) may be partly due to the bones of *Chiroptera*, which occupied the East Chamber at that time. The bone material was fully dissolved and then became partly stored as authigenic phosphates stable in acidic environments and partly moved downward with solutions to be deposited in the underlying sediments. The same layers, as well as layer 8, show abnormal concentrations of essential Cu and Zn (hundreds and thousands of ppm, respectively). The solubility of bone carbonate-bearing hydroxylapatite compared to stoichiometric hydroxylapatite is greater due to smaller sizes of crystallites, increased lattice disorder, and impurities, and it becomes increasingly soluble with decreasing pH [107].

Proceeding from the above data, the presence of intact bone material may be expected in Holocene layers 6, 7, and 8 in a narrow strip of sediments abutting the cave walls. Because bats avoid steep walls and low ceilings [39,40,106] and no lateral or upward spread of phosphate solutions was observed along layers toward the cave walls within the sampled section, one may expect that bone material in the near-wall space had a chance to survive.

8. Conclusions

Assemblages of authigenic phosphates and their distribution were studied in the Late Pleistocene–Early Holocene sedimentary sequence of Denisova Cave, located in the Altai region, South Siberia. The rich phosphatic profile was documented to a depth of 1.5 m, where eight phosphate minerals were identified, which allowed for reconstruction of some parameters that controlled dissolution/precipitation reactions and the resulting mineral assemblages. A set of mineralogical and geochemical data led to important archeological implications.

The formation of authigenic phosphates in the sediments of the East Chamber was mainly driven by biodegradation of several ≥2 m thick layers of bat guano in the lower parts of the Holocene section. The phosphate formation pathways consisted in the biodegradation of organic matter (mainly insectivorous bat guano), its P-rich acidic leaching, and gradual neutralization.

The primary layers of bat guano in the cave deposits of the East Chamber have several markers: (i) partially degraded N-rich organic matter; (ii) insect exoskeletons; (iii) extremely high S, P, Zn, and Cu enrichment of bulk sediments; (iv) assemblages of authigenic phosphates stable in acidic environments (ardealite, taranakite, and leucophosphite). Therefore, large colonies of insectivorous bats lived for a long time in the East Chamber of Denisova Cave during the deposition of layers 6 (top), 7, and 8. That time interval is bracketed between the available 9495 ± 390 yr BP and 4.5 kyr BP 14C ages of sediments from the top of layer 8 and layer 5, respectively [30].

Bone material soluble in acidic pore waters was another key source of phosphorus in layers 6 and 7. Phosphorus was partly immobilized in the top layers as authigenic phosphates stable under acidic conditions and partly moved down with neutralized solutions to redeposit as phosphates stable under slightly acidic or nearly neutral pH.

The column of layers 6–11.2 shows a particular geochemical profile corresponding to the profile of authigenic phosphate minerals. The stable assemblages of phosphate minerals are ardealite, taranakite, and leucophosphite at the top of the section, which formed by acidic leaching during biodegradation of bat guano; whitlockite, brushite, and hydroxylapatite of low crystallinity stable at slightly acidic and neutral pH in the middle layers; and only hydroxylapatite coexisting with calcite at the bottom of the leaching profile. This profile with pH values varying from 3 to 8 remained preserved in the sediments due to the hydrological regime of the prehistoric cave, which was warm and dry during the bat occupation.

Acidic leaching is mainly responsible for damage and/or elimination of archaeological and/or paleontological materials in layers 6–8 and especially in layer 9 that was affected by at least three main acidic waves. This process creates problems for OSL and radiocarbon dating, as well as for genetic analyses of bone materials of these layers [32,97–100]. Well-preserved, archaeologically valuable material in the layers affected by acidic phosphate leaching can be found in narrow strips of sediments abutting the cave walls.

The reported results open a new perspective on the interaction of humans with their environment, at least in North Asia. Authigenic phosphates can be used successfully as markers of cave paleoenvironments in territories of cold and wet climates. Taranakite can survive after complete degradation of guano layers in nearly neutral environments, especially in layers additionally enriched with bone material. The upper level, where taranakite can exist in archaeological sections, marks the position of the primary guano layers and hence the stratigraphic boundaries of bat occupation. The data on the pH-contrasting phosphate profile in the East Chamber of Denisova Cave provided proofs that the cave was abandoned by people in the earliest Holocene for unknown reasons and became occupied by large colonies of insectivorous bats.

The case of cave deposits from the East Chamber was used to develop a strategy for detecting the intervals of paleochemistry and paleoenvironments that correspond to archaeologically significant events. The same strategy can be applied to any caves located in similar conditions. So far, such studies have been mainly performed in zones of hot, arid (Israel) Mediterranean (Greece, France) or temperate (Romania) climates (Table 1).

Author Contributions: Project idea: E.V.S., M.B.K., M.V.S., S.N.K. and N.A.K.; conceptualization: E.V.S., M.B.K., S.N.K. and A.V.N.; field work: M.B.K., M.V.S. and N.A.K.; SEM analyses: E.V.S., V.A.D. and A.V.N.; XRD analysis: P.V.K.; interpretation of analytical data: E.V.S., S.N.K. and A.V.N.; visualization: A.V.N., M.B.K. and S.N.K.; writing: E.V.S., S.N.K. and M.B.K. All authors have read and agreed to the published version of the manuscript.

Funding: Archaeological investigations were supported by the Russian Science Foundation (grant number 22-28-00049). SEM and XRD studies of phosphate mineralization were carried out as part of a government assignment to the V.S. Sobolev Institute of Geology and Mineralogy (Novosibirsk).

Data Availability Statement: The data set is presented directly in the present study.

Acknowledgments: We kindly appreciate fruitful scientific collaboration with our colleagues, Yurii V. Seryotkin and Mikhail V. Khlestov, from V.S. Sobolev Institute of Geology and Mineralogy (Novosibirsk). Special thanks to T. Perepelova for helpful advice.

Conflicts of Interest: The authors declare no conflict of interest.

References

1. Shahack-Gross, R.; Berna, F.; Karkanas, P.; Weiner, S. Bat guano and preservation of archaeological remains in cave sites. *J. Archeol. Sci.* **2004**, *31*, 1259–1272. https://doi.org/10.1016/j.jas.2004.02.004.

2. Karkanas, P. Preservation of anthropogenic materials under different geochemical processes: A mineralogical approach. *Quat. Int.* **2010**, *214*, 63–69. https://doi.org/10.1016/j.quaint.2009.10.017.
3. Wurster, C.M.; Munksgaard, N.; Zwart, C.; Bird, M. The biogeochemistry of insectivorous cave guano: A case study from insular Southeast Asia. *Biogeochemistry* **2015**, *124*, 163–175. https://doi.org/10.1007/s10533-015-0089-0.
4. Shunkov, M.V.; Kulik, N.A.; Kozlikin, M.B.; Sokol, E.V.; Miroshnichenko, L.V.; Ulianov, V.A. The phosphates of Pleistocene-Holocene sediments of the Eastern Gallery of Denisova Cave. *Doklady Earth Sci.* **2018**, *478*, 46–50. https://doi.org/10.1134/S1028334X18010270.
5. Birkeland, P.W. *Soils and Geomorphology*; Oxford Univ. Press: New York, NY, USA, 1999; 430p.
6. Bohn, H.L.; Myer, R.A.; O'Connor, G.A. *Soil Chemistry*; John Wiley & Sons: Oxford, UK, 2002.
7. Retallack, G.J. *Soils of The Past: An Introduction to Paleopedology*; Blackwell: Oxford, UK, 2001; 600p.
8. Canti, M.; Huisman, D.J. Scientific advances in geoarchaeology during the last twenty years. *J. Archeol. Sci.* **2015**, *56*, 96–108. https://doi.org/10.1016/j.jas.2015.02.024.
9. Derevianko, A.P.; Shunkov, M.V.; Agadjanian, A.K.; Baryshnikov, G.F.; Malaeva, E.M.; Ulianov, V.A.; Kulik, N.A.; Postnov, A.V.; Anoikin, A.A. *Paleoenvironment and Paleolithic Human Occupation of Gorny Altai*; Derevianko, A.P.; Shunkov, M.V., Eds.; Institute of Archeology and Ethnography of the Siberian Branch of the Russian Academy of Sciences: Novosibirsk, Russia, 2003, 448p. (In Russian).
10. Derevianko, A.P.; Shunkov, M.V.; Kozlikin, M.B. Who Were the Denisovans? *Archeol. Ethnol. Anthropol. Eurasia* **2020**, *48*, 3–32. https://doi.org/10.17746/1563-0110.2020.48.3.003-032.
11. Karkanas, P.; Goldberg, P. Site formation processes at Pinnacle point Cave 13B (Mossel Bay, Western Cape Province, South Africa): Resolving stratigraphic and depositional complexities with micromorphology. *J. Hum. Evol.* **2010**, *59*, 256–273. https://doi.org/10.1016/j.jhevol.2010.07.001.
12. Henderson, P.; Marlow, C.A.; Molleson, T.; Williams, C.T. Patterns of chemical change during bone fossilization. *Nature* **1983**, *306*, 358–360. https://doi.org/10.1038/306358a0.
13. Kohn, M.J.; Cerling, T.E. Stable isotope compositions of biological apatite. In *Phosphates-Geochemical, Geobiological, and Materials Importance*; Kohn, M.J., Rakovan, J., Hughes, J.M., Eds.; Mineralogical Society of America and Geochemical Society: Washington, DC, USA, 2002; pp. 455–488.
14. Kohn, M.J. Models of diffusion-limited uptake of trace elements in fossils and rates of fossilization. *Geochim. et Cosmochim. Acta* **2008**, *72*, 3758–3770. https://doi.org/10.1016/j.gca.2008.05.045.
15. Trueman, C.N.; Tuross, N. Trace elements in modern and ancient bone. In *Phosphates-Geochemical, Geobiological, and Materials Importance*; Kohn, M.J., Rakovan, J., Hughes, J.M., Eds.; Mineralogical Society of America and Geochemical Society: Washington, DC, USA, 2002; pp. 489–522.
16. Cid, A.S.; Anjos, R.M.; Zamboni, C.B.; Cardoso, R.; Muniz, M.; Corona, A.; Valladares, D.L.; Kovacs, L.; Macario, K.; Perea, D.; et al. Na, K, Ca, Mg, and U-series in fossil bone and the proposal of a radial diffusion-adsorption model of uranium uptake. *J. Env. Radioact.* **2014**, *136*, 131–139. https://doi.org/10.1016/j.jenvrad.2014.05.018.
17. Keely, H.C.M.; Hudson, G.E.; Evans, J. Trace element contents of human bones in various states of preservation. 1. The soil silhouette. *J. Archeol. Sci.* **1977**, *4*, 19–24.
18. Hedges, R.E.; Millard, A.R. Bones and groundwater: Towards the modelling of diagenetic processes. *J. Archeol. Sci.* **1995**, *22*, 155–164. https://doi.org/10.1006/jasc.1995.0017.
19. Berna, F.; Matthews, A.; Weiner, S. Solubilities of bone mineral from archaeological sites: The recrystallization window. *J. Archeol. Sci.* **2004**, *31*, 867–882. https://doi.org/10.1016/j.jas.2003.12.003.
20. Karkanas, P.; Bar-Yosef, O.; Goldberg, P.; Weiner, S. Diagenesis in prehistoric caves: The use of minerals that form in situ to assess the completeness of the archaeological record. *J. Archeol. Sci.* **2000**, *27*, 915–929. https://doi.org/10.1006/jasc.1999.0506.
21. Weiner, S.; Goldberg, P.; Bar-Yosef, O. Bone preservation in Kebara Cave, Israel using on-site Fourier transform infrared spectrometry. *J. Archeol. Sci.* **1993**, *20*, 613–627. https://doi.org/10.1006/jasc.1993.1037.
22. Onac, B.P.; Breban, R.; Kearns, J.; Tamas, T. Unusual minerals related to phosphate deposits in Cioclovina Cave, Sureanu Mts. (Romania). *Theor. Appl. Karstol.* **2002**, *15*, 27–34.
23. Onac, B.P.; Forti, P. Minerogenetic mechanisms occurring in the cave environment: An overview. *Int. J. Speleol.* **2011**, *40*, 79–98. https://doi.org/10.5038/1827-806X.40.2.1.
24. Audra, P.; De Waele, J.; Bentaleb, I.; Chroňáková, A.; Krištůfek, V.; D'Angeli, I.M.; Carbone, C.; Madonia, G.; Vattano, M.; Scopelliti, G.; et al. Guano-related phosphaterich minerals in European caves. *Int. J. Speleol.* **2019**, *48*, 75–105. https://doi.org/10.5038/1827-806X.48.1.2252.
25. Krause, J.; Fu, Q.; Good, J.M.; Viola, B.; Shunkov, M.V.; Derevianko, A.P.; Pääbo, S. The Complete Mitochondrial DNA Genome of an Unknown Hominin from Southern Siberia. *Nature* **2010**, *464*, 894–897. https://doi.org/10.1038/nature08976.
26. Reich, D.; Green, R.E.; Kircher, M.; Krause, J.; Patterson, N.; Durand, E.Y.; Viola, B.; Briggs, A.W.; Stenzel, U.; Johnson, P.L.F.; et al. Genetic history of an archaic hominin group from Denisova Cave in Siberia. *Nature* **2010**, *468*, 1053–1060. https://doi.org/10.1038/nature09710.

27. Meyer, M.; Kircher, M.; Gansauge, M.-T.; Li, H.; Racimo, F.; Mallick, S.; Schraiber, J.G.; Jay, F.; Prüfer, K.; Filippo, C.d.; et al. A High-Coverage Genome Sequence from an Archaic Denisovan Individual. *Science* **2012**, *338*, 222–226. https://doi.org/10.1126/science.1224344.
28. Slon, V.; Mafessoni, F.; Vernot, B.; de Filippo, C.; Grote, S.; Viola, B.; Hajdinjak, M.; Peyrégne, S.; Nagel, S.; Brown, S.; et al.The genome of the offspring of a Neanderthal mother and a Denisovan father. *Nature* **2018**, *561*, 113–116. https://doi.org/10.1038/s41586-018-0455-x.
29. Okladnikov, A.P.; Ovodov, N.D. Denisova Cave paleolithic site in Altai Mountains. In *Archaeological Discoveries 1977*; Rybakov, B.A., Ed.; Nauka: Moscow, Russia, 1978, pp. 266–268. (In Russian)
30. Derevianko, A.P.; Molodin, V.I. *Denisova Cave*; Nauka: Novosibirsk, Russia, 1994, 262p. (In Russian)
31. Derevianko, A.P.; Shunkov, M.V.; Anoikin, A.A.; Ulyanov, A.V. The upper paleolithic of Denisova Cave: New results. In *Problems of Archaeology, Ethnography, Anthropology of Siberia and Neighboring Territorie*s; Derevianko, A.P., Molodin, V.I., Eds.; Institute of Archeology and Ethnography of the Siberian Branch of the Russian Academy of Sciences: Novosibirsk, Russia, 2000; Volume 6, pp. 93–98. (In Russian)
32. Jacobs, Z.; Li, B.; Shunkov, M.V.; Kozlikin, M.B.; Bolikhovskaya, N.S.; Agadjanian, A.K.; Uliyanov, V.A.; Vasiliev, S.K.; O'Gorman, K.; Derevianko, A.P.; et al. Timing of archaic hominin occupation of Denisova Cave in southern Siberia. *Nature* **2019**, *565*, 594–599. https://doi.org/10.1038/s41586-018-0843-2.
33. Filippov, A.G. Denisova Cave. In *Atlas of the Caves of Russia;* Shelepin, A.L., Ed.; Russian Geographical Society, Russian Union of Speleologist: Moscow, Russia, 2019; pp. 485–487. (In Russian)
34. Vistingauzen, V.K. Speleological zoning of Altai. *Bull. AB RGS* **2019**, *1*, 17–27. https://doi.org/10.24411/2410-1192-2019-15202. (In Russian)
35. Marinin, A.M. *Karst and Caves of Altai*; Novosibirsk State Pedagogical University: Novosibirsk, Russia, 1990; 148p. (In Russian)
36. Bolikhovskaya, N.S.; Kozlikin, M.B.; Shunkov, M.V.; Ulianov, V.A.; Faustov, S.S. New data in palynology of unique Paleolithic site Denisova Cave in the North-Western Altai. *Bull. Moscow Soc. Nat. Biol. Ser.* **2017**, *122*, 46–60. (In Russian)
37. Shunkov, M.V.; Agadzhanyan, A.K. Microclimate of Denisova Cave. In *Problems of Archaeology, Ethnography, Anthropology of Siberia and Neighboring Territories*; Derevianko, A.P., Molodin, V.I., Eds.; Institute of Archeology and Ethnography of the Siberian Branch of the Russian Academy of Sciences: Novosibirsk, Russia, 2007; Volume 13, pp. 162–166. (In Russian)
38. Vasenkov, D.A. *Chiroptera Mammalia* in highliands of southwestern Siberia. Ph.D. Thesis, Institute of Systematics and Ecology of Animals, Novosibirsk, Russia, 2009. (In Russian)
39. Zhigalin, A.V. *Mammalia, Chiroptera, Vespertilionidae* of the Altai-Sayan Mountain Province and its Surroundings: Fauna and Ecology. Ph.D. Thesis, National Research Tomsk State University, Tomsk, Russia, 2018. (In Russian)
40. Zhigalin, A.V.; Gadzhiev, A.A.; Daudova, M.G.; Salimkhanov, N.G.; Shestopalov, A.M. Ecology of chiroptera bats in Altai-Sayan region of Southern Siberia. *S. Russ. Ecol. Develop.* **2019**, *14*, 9–25. https://doi.org/10.18470/1992-1098-2019-1-9-25 (In Russian)
41. Leonov, A.V.; Bobkov, A.E.; Baturin, Y.M.; Anikushkin, M.N.; Rys, I.V.; Kozlikin, M.B.; Shunkov, M.V.; Derevianko, A.P. Development of a virtual 3d model of Denisova Cave in the Altai mountains. *Archeol. Ethnol. Anthropol. Eurasia* **2014**, *3*, 14–20.
42. Wilson, M.J.; Bain, D.C. Occurrence of leucophosphite in a soil from Elephant Island, British Antarctic Territory. *Am. Mineral.* **1976**, *61*, 1027–1028.
43. Simas, F.N.B.; Schaefer, C.E.G.R.; Melo, V.F.; Albuquerque-Filho, M.R.; Michel, R.F.M.; Pereira, V.V.; Gomes, M.R.M.; da Costa, L.M. Ornithogenic cryosols from maritime Antarctica: Phosphatization as a soil forming process. *Geoderma* **2007**, *138*, 191–203. https://doi.org/10.1016/j.geoderma.2006.11.011.
44. McFarlane, D.A.; Keeler, R.C.; Mizutani, H. Ammonia volatilization in a Mexican bat cave ecosystem. *Biogeochem* **1995**, *30*, 1–8. https://doi.org/10.1007/BF02181037.
45. Karkanas, P.; Rigaud, J.P.; Simek, J.F.; Albert, R.M.; Weiner, S. Ash bones and guano: A study of the minerals and phytoliths in the sediments of Grotte XVI, Dordogne, France. *J. Archeol. Sci.* **2002**, *29*, 721–732. https://doi.org/10.1006/jasc.2001.0742.
46. Fiore, S.; Laviano, R. Brushite, hydroxylapatite, and taranakite from Apulian caves (southern Italy): New mineralogical data. *Am. Mineral.* **1991**, *76*, 1722–1727.
47. Rellini, I.; Firpo, M.; Martino, G.; Riel-Salvatore, J.; Maggi, R. Climate and environmental changes recognized by micromorphology in Paleolithic deposits at Arene Candide (Liguria, Italy). *Quat. Int.* **2013**, *315*, 42–55. https://doi.org/10.1016/j.quaint.2013.05.050.
48. Forbes, M.S.; Bestland, E.A. Guano-derived deposits within the sandy cave fills of Naracoorte, South Australia. *Alcheringa: Australas. J. Palaeontol.* **2006**, *30*, 129–146. https://doi.org/10.1080/03115510609506859.
49. Onac, B.P.; Vereş, D.S. Sequence of secondary phosphates deposition in a karst environment: Evidence from Magurici Cave (Romania). *Europ. J. Mineral.* **2003**, *15*, 741–745. https://doi.org/10.1127/0935-1221/2003/0015-0741.
50. Dumitraş, D.G.; Marincea, Ş.; Bilal, E.; Hatert, F. Apatite-(CaOH) in the fossil bat guano deposit from the "dry" Cioclovina Cave, Sureanu Mountains, Romania. *Can. Mineral.* **2008**, *46*, 431–445. https://doi.org/10.3749/canmin.46.2.431.
51. Marincea, Ş.; Dumitraş; D.G.; Diaconu, G.; Bilal, E. Hydroxylapatite, brushite and ardealite in the bat guano deposit from Peştera Mare de la Mereşti, Perşani Mountains, Romania. *Neues Jahrb. für Mineral. Abhandlungen* **2004**, *10*, 464–488.

52. Dumitraş, D.G.; Marincea, Ş. Sequential dehydration of the phosphate-sulfate association from Gura Dobrogei Cave, Dobrogea, Romania. *Europ. J. Mineral.* **2021**, *33*, 329–340. https://doi.org/10.5194/ejm-33-329-2021.
53. Tămaş, T.; Miheţ, O.; Giurgiu, A. Mineralogy of bat guano deposits from Huda lui Papară cave (Trascău Mountains, Romania). *Carpath. J. Earth Env. Sci.* **2014**, *9*, 25–32.
54. Dumitraş, D.G.; Marincea, Ş.; Fransolet, A.M. Brushite in the bat guano deposit from the "dry" Cioclovina Cave (Sureanu Mountains, Romania). *Neues Jahrb. für Mineral. Abhandlungen* **2004**, *180*, 45–64. https://doi.org/10.1127/0077-7757/2004/0180-0045.
55. Onac, B.P.; Sumrall, J.; Mylroie, J.E.; Kearns, J.B. *Cave minerals of San Salvador Island, Bahamas*; University of South Florida: Tampa Library: Tampa, FL, USA, 2009; 70p.
56. Snow, M.R.; Pring, A.; Allen, N. Minerals of the Wooltana Cave, Flinders Ranges, South Australia. *Trans. R. Soc. S. Aust.* **2014**, *138*, 214–230. https://doi.org/10.1080/03721426.2014.11649009.
57. Dumitraş, D.G. A re-investigation of ardealite from the type locality, the "dry" Cioclovina Cave (Şureanu Mountains, Romania). *Europ. J. Mineral.* **2017**, *529*, 1055–1066. https://doi.org/10.1127/ejm/2017/0029-2655.
58. Goldberg, P.S.; Nathan, Y. The phosphate mineralogy of et-Tabun cave, Mount Carmel, Israel. *Mineral. Mag.* **1975**, *40*, 253–258. https://doi:10.1180/minmag.1975.040.311.06.
59. Quattropani, L.; Charlet, L.; De Lumley, H.; Menu, M. Early Palaeolithic bone diagenesis in the Arago cave at Tautavel, France. *Mineral. Mag.* **1999**, *63*, 801–812. https://doi.org/10.1180/002646199548943.
60. Onac, B.P.; Kearns, J.; Breban, R.; Cîntă Pânzaru, S. Variscite ($AlPO_4{\cdot}2H_2O$) from Cioclovina Cave (Sureanu Mountains, Romania): A tale of a missing phosphate. *Studia UBB Geol.* **2004**, *49*, 3–14. https://doi.org/10.5038/1937-8602.49.1.1.
61. Giurgiu, A.; Tămaş, T. Mineralogical data on bat guano deposits from three Romanian caves. *Studia UBB Geol.* **2013**, *58*, 13–18. https://doi.org/10.5038/1937-8602.58.2.2.
62. Marincea, Ş.; Dumitraş, D.G. The occurrence of taranakite in the in the "dry" Cioclovina Cave (Sureanu Mountains, Romania). *Neues Jahrb. für Mineral. Abhandlungen* **2003**, *3*, 127–144. https://doi.org/10.1127/0028-3649/2003/2003-0127.
63. Dumitraş, D.G.; Marincea, Ş.; Diaconu, G. Leucophosphite and taranakite in the bat-guano deposit from Lazului Cave (Mehedinți Mountains). *Rom. J. Miner. Depos.* **2002**, *80*, 23–25.
64. Morley, M.V.; Goldberg, P.; Uliyanov, V.A.; Kozlikin, M.B.; Shunkov, M.V.; Derevianko, A.P.; Jacobs, Z.; Roberts, R.G. Hominin and animal activities in the microstratigraphic record from Denisova Cave (Altai Mountains, Russia). *Sci. Rep*. **2019**, *9*, 13785. https://doi.org/10.1038/s41598-019-49930-3.
65. Ulyanov, V.A.; Shunkov, M.V. Some features of sedimentation in the East Chamber of Denisova Cave. In *Problems of Archaeology, Ethnography, Anthropology of Siberia and Neighboring Territories*; Derevianko, A.P., Molodin, V.I., Eds.; Institute of Archeology and Ethnography of the Siberian Branch of the Russian Academy of Sciences: Novosibirsk, Russia, 2013; Volume 19, pp. 159–162 (In Russian).
66. Agadzhanyan, A.K.; Shunkov, M.V.; Kozlikin, M.B. Small Vertebrates from the Pleistocene Sediments of the East Chamber of Denisova Cave, Northwestern Altai Mountains. *Paleontol. J.* **2021**, *55*, 331–342. https://doi.org/10.1134/S0031030121030035.
67. Vasiliev, S.K.; Kozlikin, M.B.; Shunkov, M.V. Megafaunal Remains from the upper portion of pleistocene deposits in South Chamber of Denisova Cave. In *Problems of Archaeology, Ethnography, Anthropology of Siberia and Neighboring Territories*; Derevianko, A.P., Molodin, V.I., Eds.; Institute of Archeology and Ethnography of the Siberian Branch of the Russian Academy of Sciences: Novosibirsk, Russia, 2018; Volume 24, pp. 37–41. (In Russian)
68. Derevianko, A.P.; Shunkov, M.V.; Kozlikin, M.B.; Ulyanov, V.A.; Chekha, A.M. The upper Paleolithic of the East Chamber in Denisova Cave: New data. In *Problems of Archaeology, Ethnography, Anthropology of Siberia and Neighboring Territories*; Derevianko, A.P., Molodin, V.I., Eds.; Institute of Archeology and Ethnography of the Siberian Branch of the Russian Academy of Sciences: Novosibirsk, Russia, 2014; Volume 20, pp. 50–53. (In Russian)
69. Sokol, E.V.; Kokh, S.N.; Kozmenko, O.A.; Lavrushin, V.Y.; Belogub, E.V.; Khvorov, P.V.; Kikvadze, O.E. Boron in an onshore mud volcanic environment: Case study from the Kerch Peninsula, the Caucasus continental collision zone. *Chem. Geol.* **2019**, *525*, 58–81. https://doi.org/10.1016/j.chemgeo.2019.07.018.
70. Shatsky, V.; Sitnikova, E.; Kozmenko, O.; Palessky, S.; Nikolaeva, I.; Zayachkovsky, A. Behavior of incompatible elements during ultrahigh-pressure metamorphism (by the example of rocks of the Kokchetav massif). *Russ. Geol. Geophys.* **2006**, *47*, 482–496.
71. Sakae, T.; Nagata, H.; Sudo, T. The crystal structure of synthetic calcium phosphate-sulfate hydrate, $Ca_2HPO_4SO_4{\cdot}4H_2O$, and its relation to brushite and gypsum. *Am. Mineral.* **1978**, *63*, 520–527.
72. Sakae, T.; Sudo, T. Taranakite from the Onino-Iwaya limestone cave at Hiroshima Prefecture, Japan: A new occurrence. *Am. Mineral.* **1975**, *60*, 331–334.
73. Capitelli, F.; Bosi, F.; Capelli, S.C.; Radica, F.; Della Ventura, G. Neutron and XRD single-crystal diffraction study and vibrational properties of whitlockite, the natural counterpart of synthetic tricalcium phosphate. *Crystals* **2021**, *11*, 225. https://doi.org/10.3390/cryst11030225.
74. International Centre for Diffraction Data. *PDF-4+. Powder Diffraction File*; Windows; International Centre for Diffraction Data: Newtown Square, PA, USA, 2009.
75. Xu, G.; Aksay, I.A.; Groves, J.T. Continuous crystalline carbonate apatite thin films. A biomimetic approach. *J. Am. Chem. Soc.* **2001**, *123*, 2196–2203. https://doi.org/10.1021/ja002537i.

76. Goldberg, M.A.; Krohicheva, P.A.; Fomin, A.S.; Khairutdinova, D.R.; Antonova, O.S.; Baikin, A.S.; Smirnov, V.V.; Fomina, A.A.; Leonov, A.V.; Mikheev, I.V.; et al. In situ magnesium calcium phosphate cements formation: From one pot powders precursors synthesis to in vitro investigations. *Bioact. Mater.* **2020**, *5*, 644–658. https://doi.org/10.1016/j.bioactmat.2020.03.011.
77. Cacciotti, I. Cationic and anionic substitutions in hydroxyapatite. In *Handbook of Bioceramics and Biocomposites*; Springer: Berlin/Heidelberg, Germany, 2016; pp. 145–211.
78. Beaufils, S.; Rouillon, T.; Millet, P.; Le Bideau, J.; Weiss, P.; Chopart, J.P.; Daltin, A.L. Synthesis of calcium-deficient hydroxyapatite nanowires and nanotubes performed by template-assisted electrodeposition. *Mater. Sci. Engineer. C* **2019**, *98*, 333–346.
79. Minh, D.P.; Tran, N.D.; Nzihou, A.; Sharrock, P. Carbonate-containing apatite (CAP) synthesis under moderate conditions starting from calcium carbonate and orthophosphoric acid. *Mater. Sci. Eng. C* **2013**, *33*, 2971–2980. https://doi.org/10.1016/j.msec.2013.03.023.
80. Li, J. Structural characterisation of apatite-like materials. Ph.D. Thesis, University of Birmingham, Birmingham, UK, 2010.
81. International Centre for Diffraction Data. *PDF-2. Powder Diffraction File*; Windows; Newtown Square: International Centre for Diffraction Data: Newtown Square, PA, USA, 2005.
82. Markin, S.V. Natural scientific and archaeological evidence from the pleistocene layers of Kaminnaya cave. In *Problems of Archaeology, Ethnography, Anthropology of Siberia and Neighboring Territories*; Derevianko, A.P., Ed.; Institute of Archeology and Ethnography of the Siberian Branch of the Russian Academy of Sciences: Novosibirsk, Russia, 2021; Volume 26, pp. 182–187;. https://doi.org/10.17746/2658-6193.2021.27.0182-0187. (In Russian)
83. Derevianko, A.P.; Glinskii, S.V.; Dergacheva, M.I.; Dupal, T.A.; Efremov, S.A.; Zenin, A.N.; Krivoshapkin, A.I.; Kulikov, O.I.; Malaeva, E.M.; Markin, S.V.; et al. *The Problems of Paleoecology, Geology and Archaeology of the Paleolithic of the Altai*; Institute of Archeology and Ethnography of the Siberian Branch of the Russian Academy of Sciences: Novosibirsk, Russia, 1998, 312p. (In Russian).
84. Nriagu, J.O. Phosphate-clay mineral relations in soils and sediments. *Can. J. Earth Sci.* **1976**, *13*, 717–736. https://doi.org/10.1139/e76-077.
85. Savenko, A.V. The possibility of phosphatization of silicates in the supergene zone. *Geochem. Int.* **2015**, *53*, 87–94. https://doi.org/10.1134/S001670291501005X.
86. Roncal-Herrero, T.; Oelkers, E.H. Does variscite control phosphate availability in acidic natural waters? An experimental study of variscite dissolution rates. *Geochim. et Cosmochim. Acta* **2011**, *75*, 416–426. https://doi.org/10.1016/j.gca.2010.10.012.
87. Liu, P.L.; Sherman, G.D.; Swindale, L.D. Laboratory formation and characterization of taranakite in a hydrol humic Latosol soil from Hawaii. *Pacific Sci.* **1966**, *20*, 496–506.
88. Karkanas, P.; Kyparissi-Apostolika, N.; Bar-Yosef, O.; Weiner, S. Mineral assemblages in Theopetra, Greece: A framework for understanding diagenesis in a prehistoric cave. *J. Archeol. Sci.* **1999**, *26*, 1171–1180.
89. Krauskopf, K.B.; Bird, D.K. *Introduction to Geochemistry*; McGraw-Hill Book Company: New York, NY, USA, 1979; 617p.
90. Eltantawy, M.M.; Belokon, M.A.; Belogub, E.V.; Ledovich, O.I.; Skorb, E.V.; Ulasevich, S.A. Self-Assembled Liesegang Rings of Hydroxyapatite for Cell Culturing. *Adv. NanoBiomed Res.* **2021**, *1*, 2000048. https://doi.org/10.1002/anbr.202000048.
91. Kizalaite, A.; Grigoraviciute-Puroniene, I.; Asuigui, D.R.C.; Stoll, S.L.; Cho, S.H.; Sekino, T.; Kareiva, A.; Zarkov, A. Dissolution-Precipitation Synthesis and Characterization of Zinc Whitlockite with Variable Metal Content. *ACS Biomater. Sci. Eng.* **2021**, *7*, 3586–3593. https://doi.org/10.1021/acsbiomaterials.1c00335.
92. Zhou, J.M.; Liu, C.; Huang, P.M. Perturbation of taranakite formation by ferrous and ferric iron under acidic conditions. *Soil Sci. Soc. Am. J.* **2000**, *64*, 885–892. https://doi.org/10.2136/sssaj2000.643885x.
93. Toshima, T.; Hamai, R.; Tafu, M.; Takemura, Y.; Fujita, S.; Chohji, T.; Tanda, S.; Li, S.; Qin, G.W. Morphology control of brushite prepared by aqueous solution synthesis. *J. Asian. Ceram. Soc.* **2014**, *2*, 52–56. https://doi.org/10.1016/j.jascer.2014.01.004.
94. Veresov, A.G.; Putlyaev, V.I.; Tret'yakov, Y.D. Chemistry of calcium phosphate-based inorganic materials. *Ross. Khim. Zh.* **2004**, *48*, 52–63. (In Russian)
95. Boanini, E.; Silingardi, F.; Gazzano, M.; Bigi, A. Synthesis and hydrolysis of brushite (DCPD): The role of ionic substitution. *Crystal Growth Design* **2021**, *21*, 1689–1697.
96. Vasiliev, S.K.; Shunkov, M.V.; Kozlikin, M.B. Pleistocene climate in the Northwestern Altai reconstructed from megafauna fossils in the East Chamber of Denisova Cave. In *Problems of Archaeology, Ethnography, Anthropology of Siberia and Neighboring Territories*; Derevianko, A.P., Molodin, V.I., Eds.; Institute of Archeology and Ethnography of the Siberian Branch of the Russian Academy of Sciences: Novosibirsk, Russia, 2017; Volume 23; pp. 60–64. (In Russian)
97. Brown, S.; Kozlikin, M.; Shunkov, M.; Derevianko, A.; Higham, T.; Douka, K.; Korzow Richter, K. Examining collagen preservation through glutamine deamination at Denisova Cave. *J. Archeol. Sci.* **2021**, *133*, 105454. https://doi.org/10.1016/j.jas.2021.105454.
98. Brown, S.; Wang, N.; Oertle, A.; Kozlikin, M.B.; Shunkov, M.V.; Derevianko, A.P.; Comeskey, D.; Jope-Street, B.; Harvey, V.L.; Chowdhury, M.P.; et al. Zooarchaeology through the lens of collagen fingerprinting at Denisova Cave. *Sci. Rep.* **2021**, *11*, 15457. https://doi.org/10.1038/s41598-021-94731-2.
99. Zavala, E.I.; Jacobs, Z.; Vernot, B.; Shunkov, M.V.; Kozlikin, M.B.; Derevianko, A.P.; Essel, E.; Fillipo, de C.; Nagel, S.; Richter, J.; Romagné, F.; et al. Pleistocene sediment DNA reveals hominin and faunal turnovers at Denisova Cave. *Nature* **2021**, *595*, 399–403. https://doi.org/10.1038/s41586-021-03675-0.

100. Massilani, D.; Morley, M.W.; Mentzer, S.M.; Aldeias, V.; Vernot, B.; Miller, Ch.; Stahlschmidt, M.; Kozlikin, M.B.; Shunkov, M.V.; Derevianko, A.P.; Conard, N.J.; et al. Microstratigraphic preservation of ancient faunal and hominin DNA in Pleistocene cave sediments. *PNAS* **2022**, *119*, e2113666118. https://doi.org/10.1073/pnas.2113666118.
101. Kulik, N.A.; Kozlikin, M.B.; Miroshnichenko, L.V.; Shunkov, M.V. Impact of phosphate mineralization of sediments on the preservation of stone artifacts (based on evidence from Denisova Cave). In *Problems of Archaeology, Ethnography, Anthropology of Siberia and Neighboring Territories*; Derevianko, A.P., Ed.; Institute of Archeology and Ethnography of the Siberian Branch of the Russian Academy of Sciences: Novosibirsk, Russia, 2020; Volume 24; pp. 142–147;. https://doi.org/10.17746/2658-6193.2020.26.142-147 (In Russian).
102. Agadzhanyan, A.K.; Rosina, V.V. Bats from the Pleistocene deposits of Denisova Cave. In *Problems of Archaeology, Ethnography, Anthropology of Siberia and Neighboring Territories*; Derevianko, A.P., Molodin, V.I., Eds.; Institute of Archeology and Ethnography of the Siberian Branch of the Russian Academy of Sciences: Novosibirsk, Russia, 2001; Volume 8; pp. 33–36 (In Russian)
103. Agadzhanyan, A.K.; Rosina, V.V.; Shunkov, M.V. The role of bats in the Pleistocene biogeny of the Denisova Cave area. In *Problems of Archaeology, Ethnography, Anthropology of Siberia and Neighboring Territories*; Derevianko, A.P., Molodin, V.I., Eds.; Institute of Archeology and Ethnography of the Siberian Branch of the Russian Academy of Sciences: Novosibirsk, Russia, 2004; Volume 10; pp. 6–11. (In Russian)
104. Rosina, V.V. The Pleistocene and Holocene History of *Chiroptera Mammalia* fauna in the Northwestern Altai. Ph.D. Thesis, Paleontological Institute of Russian Academy of Sciences, Moscow, Russia, 2004. (In Russian)
105. Derevianko, A.P.; Shunkov, M.V.; Fedorchenko, A.Y.; Kozlikin, M.B. A Palaeolithic diadem from Denisova Cave. In *Problems of Archaeology, Ethnography, Anthropology of Siberia and Neighboring Territories*; Derevianko, A.P., Molodin, V.I., Eds.; Institute of Archeology and Ethnography of the Siberian Branch of the Russian Academy of Sciences: Novosibirsk, Russia, 2018; Volume 24, pp. 87–90. (In Russian)
106. Bannikov, A.G.; Vtorov, P.P.; Gladkova, T.D.; Kuzyakin, A.P.; Naumov, S.P.; Novikov, G.A.; Rogacheva, E.V.; Tomilin, A.G.; Flint, V.E. Mammals, Eutheria. In *The Life of Animals, 6 Volumes;* Naumov, S.P., Kuzyakin, A.P., Eds.; Prosveshchenie: Moscow, Russia, 1971; 627p. (In Russian)
107. Constantz, B.R.; Ison, I.C.; Fulmer, M.T.; Poser, R.D.; Smith, S.T.; VanWagoner, M.; Rosssteven, J.; Goldsteinjesse, A.; Jupiter, B.; Rosenthal, D.I. Skeletal repair by in situ formation of the mineral phase of bone. *Science* **1995**, *267*, 1796–1799. https://doi.org/10.1126/science.7892603.